

# A deterministic-particle-based scheme for micro-macro viscoelastic flows

Xuelian Bao<sup>1</sup>

*School of Mathematics, South China University of Technology, Guangzhou, Guangdong 510641, People's Republic of China*

Chun Liu<sup>2</sup>

*Department of Applied Mathematics, Illinois Institute of Technology, Chicago, IL 60616, United States*

Yiwei Wang<sup>3</sup>

*Department of Mathematics, University of California, Riverside, Riverside, CA 92521, United States*

---

## Abstract

In this article, we introduce a new method for discretizing micro-macro models of dilute polymeric fluids by integrating a finite element discretization for the macroscopic fluid dynamic equation with a deterministic variational particle scheme for the microscopic Fokker-Planck equation. To address challenges arising from micro-macro coupling, we employ a discrete energetic variational approach to derive a coarse-grained micro-macro model with a particle approximation first and then develop a particle-FEM discretization for the coarse-grained model. The accuracy of the proposed method is evaluated for a Hookean dumbbell model in a Couette flow by comparing the computed velocity field with existing analytical solutions. We also use our method to study nonlinear FENE dumbbell models in different scenarios, such as extension flow, pure shear flow, and lid-driven cavity flow. Numerical examples demonstrate that the proposed deterministic particle approach can accurately capture the various key rheological phenomena in the original FENE model, including hysteresis and  $\delta$ -function-like spike behavior in extension flows, velocity overshoot phenomenon in pure shear flow, symmetries breaking, vortex center shifting and vortices weakening in the lid-driven cavity flow, with a small number of particles.

---

## 1. Introduction

Complex fluids comprise a large class of soft materials, such as polymeric solutions, liquid crystals, ionic solutions, and fiber suspensions. These are fluids with complicated rheological phenomena, arising from different “elastic” effects, such as the elasticity of deformable particles, the interaction between charged ions, and bulk elasticity endowed by polymer molecules [1]. Modeling and simulations of complex fluids have been interesting problems for a couple of decades [2, 3, 4, 5].

Mathematical models of complex fluids are typically categorized as pure macroscopic models [6, 7, 8] and micro-macro models [9, 4]. The pure macroscopic models employ an empirical constitutive equation for the stress tensor  $\tau$  to supplement the conservation laws of mass and momentum [6, 7, 8]. Examples include the Oldroyd-B model [10] and the FENE-P model [11]. This approach is advantageous due to its low computational cost, but the closed form of the constitutive equation may fail to capture the intricate flow behaviors of complex fluids, including hysteresis effects in polymeric fluids. Micro-macro models, on the other hand, couple the macroscopic conservation laws with the microscopic kinetic theory, which describes the origin of the macroscopic stress tensor [4, 9]. A typical example of a micro-macro model is the dumbbell model of a dilute polymeric fluid [4, 5]. In this model, a polymer chain is represented by an elastic dumbbell

---

<sup>1</sup>baoxuelian@scut.edu.cn

<sup>2</sup>cliu124@iit.edu

<sup>3</sup>yiweiw@ucr.edu, corresponding author

consisting of two beads connected by a single spring. The molecular configuration is characterized by an end-to-end vector of the dumbbell, represented by  $\mathbf{q} \in \mathbb{R}^d$ . The microscopic dynamics is described by a Fokker-Planck equation for the number density distribution function  $f(\mathbf{x}, \mathbf{q}, t)$  with a drift term depending on the macroscopic velocity field  $\mathbf{u}(\mathbf{x}, t)$ . Here,  $\mathbf{x} \in \Omega \subset \mathbb{R}^3$  is the macroscopic position, and  $\Omega$  is assumed to be a bounded domain with smooth boundary. The macroscopic motion of the fluid is described by a Navier-Stokes equation with elastic stress  $\boldsymbol{\tau}(\mathbf{x}, t)$  induced by the microscopic configuration of polymer chains. The corresponding micro-macro model is formulated as follows:

$$\begin{cases} \rho(\mathbf{u}_t + \mathbf{u} \cdot \nabla \mathbf{u}) + \nabla p = \eta_s \Delta \mathbf{u} + \nabla \cdot \boldsymbol{\tau}, & \boldsymbol{\tau} = \lambda_p \mathbb{E}(\nabla_{\mathbf{q}} \Psi \otimes \mathbf{q}) = \lambda_p \int_{\mathbb{R}^d} f \nabla_{\mathbf{q}} \Psi \otimes \mathbf{q} d\mathbf{q}, \\ \nabla \cdot \mathbf{u} = 0, \\ f_t + \mathbf{u} \cdot \nabla f + \nabla_{\mathbf{q}} \cdot ((\nabla \mathbf{u}) \mathbf{q} f) = \frac{2}{\zeta} \nabla_{\mathbf{q}} \cdot (f \nabla_{\mathbf{q}} \Psi) + \frac{2k_B T}{\zeta} \Delta_{\mathbf{q}} f, \end{cases} \quad (1)$$

subject to a suitable boundary condition on  $\mathbf{u}$  and  $f$ . Throughout this paper,  $\nabla$  with no indices denotes the derivation with respect to the macroscopic variable  $\mathbf{x}$  and  $\nabla_{\mathbf{q}}$  denotes the derivative with respect to the microscopic variable  $\mathbf{q}$ . Here,  $\rho > 0$  is the constant density of the fluid,  $\lambda_p > 0$  is a constant that represents the polymer density,  $k_B$  is the Boltzmann constant,  $T$  is the absolute temperature,  $\eta_s > 0$  is the solvent viscosity,  $\zeta > 0$  is a constant related to the polymer relaxation time, and  $\Psi(\mathbf{q})$  is the spring potential. Typical choices of the elastic potential  $\Psi(\mathbf{q})$  include

$$\Psi(\mathbf{q}) = \frac{1}{2} H |\mathbf{q}|^2, \quad \text{and} \quad \Psi(\mathbf{q}) = \begin{cases} -\frac{HQ_0^2}{2} \ln \left( 1 - \left( \frac{|\mathbf{q}|}{Q_0} \right)^2 \right), & |\mathbf{q}| < Q_0 \\ +\infty, & |\mathbf{q}| \geq Q_0 \end{cases} \quad (2)$$

known as Hookean and FENE (Finite Extensible Nonlinear Elastic) potentials. Here,  $H > 0$  is the elastic constant, and  $Q_0$  is the maximum dumbbell extension in FENE models. The interactions among polymer chains are neglected due to the dilute assumption. Alternatively, the microscopic dynamics can be described by a stochastic differential equation (SDE), or a Langevin equation, given by [4]

$$d\mathbf{q}(\mathbf{x}, t) = (-\mathbf{u} \cdot \nabla \mathbf{q}(\mathbf{x}, t) + (\nabla \mathbf{u}) \mathbf{q}(\mathbf{x}, t) - 2\zeta^{-1} \nabla_{\mathbf{q}} \Psi(\mathbf{q}(\mathbf{x}, t))) dt + \sqrt{4k_B T \zeta^{-1}} d\mathbf{W}_t, \quad (3)$$

where  $d\mathbf{W}_t$  is the standard multidimensional white noise. One of the important properties of the model (1) is that the solution satisfies the following energy-dissipation law (see section 2 for details):

$$\frac{d}{dt} \int_{\Omega} \left( \frac{1}{2} \rho |\mathbf{u}|^2 + \lambda_p \int_{\mathbb{R}^d} k_B T f \ln f + \Psi f d\mathbf{q} \right) d\mathbf{x} = - \int_{\Omega} \left( \eta_s |\nabla \mathbf{u}|^2 + \int_{\mathbb{R}^d} \frac{\lambda_p \zeta}{2} f |\nabla(k_B T \ln f + \Psi)|^2 d\mathbf{q} \right) d\mathbf{x}. \quad (4)$$

The energy-dissipation law plays a crucial role in understanding the underlying physics of the micro-macro model [12], as well as in establishing the well-posedness of the model [13].

Although micro-macro type models give an elegant description of the origin of the macroscopic stress tensor for various complex fluids [4, 9, 13], directly simulating micro-macro models has been a long-standing challenge. Various computational techniques have been developed to solve the micro-macro model (1) [14, 15, 16, 17, 18, 19]. The two main approaches are Langevin-equation-based stochastic simulation methods and direct simulation methods based on the microscopic Fokker-Planck equation [18]. One of the earliest Langevin-equation-based numerical methods is the CONNFFESSIT (Calculation of Non-Newtonian Flow: Finite Elements and Stochastic Simulation Technique) algorithm, which couples a finite element discretization to the macroscopic flow with a numerical solver for the microscopic SDE (3) [17, 19]. Along this direction, other stochastic approaches, such as the Lagrangian particle method (LPM) [15] and the Brownian configuration field (BCF) method [16], were proposed to reduce the variance and computational cost of the original CONNFFESSIT algorithm. Several extensions and corresponding numerical experiments have been extensively investigated in recent years [4, 20, 21, 22, 23, 24, 25]. Although stochastic approaches have been the dominant simulation methods for micro-macro models, they suffer from several shortcomings, including high computational costs and stochastic fluctuations. An alternative approach is to simulate the

Fokker-Planck equation in the configuration space directly. Examples include Galerkin spectral element technique [26, 27, 28, 29, 30] and the lattice Boltzmann technique [31, 32]. However, such methods are well suited only for polymeric models having low-dimensional configuration spaces, and the computational cost of Fokker-Planck-based methods increases rapidly for simulations in strong flows (with highly localized distribution function) or involving high-dimensional configuration spaces [18].

In the context of solving Fokker-Planck type equations, deterministic particle methods have recently gained considerable attention [33, 34, 35, 36, 37]. These methods handle the diffusion terms in the equation by using various kernel regularizations [36, 34, 35, 33]. Unlike Langevin dynamics-based stochastic particle methods, deterministic particle methods are often computationally cheap and do not suffer from stochastic fluctuations. The success of deterministic particle methods in solving Fokker-Planck equations has motivated us to develop an efficient numerical method for micro-macro models by incorporating a deterministic particle method. However, the micro-macro coupling in these models presents new challenges that need to be addressed.

The goal of this paper is to develop an efficient numerical method for micro-macro models by utilizing a deterministic particle method for solving the microscopic Fokker-Planck equation. To overcome these difficulties arising from the micro-macro coupling, we construct the numerical discretization based on the variational formulation of the model. More precisely, we apply the deterministic particle approximation at the energy-dissipation law (4) level and employ an energetic variational approach [38] to derive a coarse-grained micro-macro model with a particle approximation first. A particle-FEM discretization is developed for the coarse-grained model. Various numerical experiments have been performed to validate the new scheme via several benchmark problems. Despite its simplicity, the deterministic particle method is robust, accurate, and capable of catching various rheological behaviors of polymeric fluids. The numerical results obtained by our scheme are in agreement with those from the former work [17, 39, 25, 40, 41]. Moreover, deterministic particle discretization is often more efficient than most stochastic particle methods, where a large ensemble of realizations of the stochastic process and a step size is needed.

The rest of this article is organized as follows. In section 2, we present the basic energy-dissipation law associated with the micro-macro model (1) and show the continuous model can be derived from the energy-dissipation law using an energetic variational approach. In section 3, we employ the energetic variational approach to derive a coarse-grained particle-based micro-macro model by applying particle approximation at the energy-dissipation law level, and we construct a deterministic particle-FEM scheme for the coarse-grained model. Various numerical experiments are presented in Section 4. Finally, the concluding remarks are given in Section 5.

## 2. Preliminary

In this section, we briefly introduce an energetic variational approach (EnVarA). Motivated by non-equilibrium thermodynamics, particularly the celebrated works of Rayleigh [42] and Onsager [43, 44], the EnVarA has been successfully applied to build various mathematical models in physics, chemical engineering, and biology [12, 45]. It also serves as a valuable guideline for developing structure-preserving numerical schemes for these systems [38].

The key idea of EnVarA is to describe an isothermal and mechanically isolated system by its energy and the rate of energy dissipation over time, along with kinematic (transport) assumptions on the employed variables. The dynamics of the system, i.e., the PDE model, can be derived by combining the Least Action Principle (LAP) and the Maximum Dissipation Principle (MDP) [12]. More precisely, according to the first and second laws of thermodynamics [46, 12], an isothermal and closed system possesses an energy-dissipation law

$$\frac{d}{dt} E^{\text{total}}(t) = -\Delta(t) \leq 0. \quad (5)$$

Here,  $E^{\text{total}}$  is the total energy, which is the sum of the Helmholtz free energy  $\mathcal{F}$  and the kinetic energy  $\mathcal{K}$ ;  $\Delta(t) \geq 0$  stands for the rate of energy dissipation, which equals to the rate of entropy production in this case. Once these quantities are specified, for the energy part, one can employ the LAP, taking variation of

the action functional  $\mathcal{A}(\mathbf{x}) = \int_0^T (\mathcal{K} - \mathcal{F}) dt$  with respect to  $\mathbf{x}$  (the trajectory in Lagrangian coordinates) [47, 12], to derive the conservative force, i.e.,  $\delta\mathcal{A} = \int_0^T \int_{\Omega} (\text{force}_{\text{iner}} - \text{force}_{\text{conv}}) \cdot \delta\mathbf{x} d\mathbf{x} dt$ . For the dissipation part, one can apply the MDP, taking the variation of the Onsager dissipation functional  $\mathcal{D}$  with respect to the “rate”  $\mathbf{x}_t$ , to derive the dissipative force, i.e.,  $\delta\mathcal{D} = \int_{\Omega} \text{force}_{\text{diss}} \cdot \delta\mathbf{x}_t d\mathbf{x}$ , where the dissipation functional  $\mathcal{D} = \frac{1}{2}\Delta$  in the linear response regime [43]. Consequently, the force balance condition results in

$$\frac{\delta\mathcal{A}}{\delta\mathbf{x}} = \frac{\delta\mathcal{D}}{\delta\mathbf{x}_t}, \quad (6)$$

which is the dynamics of the system. In the case that  $\mathcal{K} = 0$ ,  $\frac{\delta\mathcal{A}}{\delta\mathbf{x}} = -\frac{\delta\mathcal{F}}{\delta\mathbf{x}}$ , then the dynamics can be written as  $\frac{\delta\mathcal{D}}{\delta\mathbf{x}_t} = -\frac{\delta\mathcal{F}}{\delta\mathbf{x}}$ , which is known as a generalized gradient flow. It is important to notice that the force balance equation (6) uses the strong form of the variational result, as the test functions may be in different spaces in the original variational weak form [12]. From a modeling perspective, one advantage of utilizing an energy-dissipation law to model a complex system, rather than equations, is that it allows for the systematic inclusion of multiscale and multiphysics coupling and completion.

### 2.1. EnVarA for a simple fluid

To illustrate the idea of EnVarA, we first consider a simple incompressible fluid, which is usually described by an incompressible Navier–Stokes equation

$$\begin{cases} \rho(\mathbf{u}_t + \mathbf{u} \cdot \nabla \mathbf{u}) + \nabla p = \eta \Delta \mathbf{u}, \\ \nabla \cdot \mathbf{u} = 0, \\ \rho_t + \nabla \cdot (\rho \mathbf{u}) = 0, \end{cases} \quad (7)$$

with a boundary condition  $\mathbf{u} = 0$  and initial conditions. Here,  $\mathbf{u}$  is the fluid velocity,  $\mathbf{u} \cdot \nabla \mathbf{u} = \sum_{j=1}^3 u_j \partial_j u_i$ ,  $\rho$  is the fluid density,  $\eta > 0$  is the viscosity, and  $p$  is the hydrodynamic pressure. Multiplying the first equation of (7) by  $\mathbf{u}$  and using the integration by parts, one can show  $\mathbf{u}$  satisfies the following energy-dissipation law

$$\frac{d}{dt} \int_{\Omega} \frac{1}{2} \rho |\mathbf{u}|^2 d\mathbf{x} = - \int_{\Omega} \eta |\nabla \mathbf{u}|^2 d\mathbf{x}, \quad (8)$$

where the kinetic energy  $\mathcal{K}$ , the free energy  $\mathcal{F}$  and the Onsager dissipation function  $\mathcal{D}$  are given by

$$\mathcal{K} = \int_{\Omega} \rho |\mathbf{u}|^2 d\mathbf{x}, \quad \mathcal{F} = 0, \quad \mathcal{D} = \int_{\Omega} \frac{1}{2} \eta |\nabla \mathbf{u}|^2 d\mathbf{x}. \quad (9)$$

The goal of EnVarA is to derive the equation of  $\mathbf{u}$ , i.e., the momentum equation in (7), from the energy-dissipation law (8) using the LAP and MDP. In more detail, to apply the LAP and MDP, one needs to introduce a Lagrangian description of the system by defining the flow map associated with the velocity field  $\mathbf{u}(\mathbf{x}, t)$  through the ordinary differential equation:

$$\frac{d}{dt} \mathbf{x}(\mathbf{X}, t) = \mathbf{u}(\mathbf{x}(\mathbf{X}, t), t), \quad \mathbf{x}(\mathbf{X}, 0) = \mathbf{X}, \quad (10)$$

where  $\mathbf{X} \in \Omega^0$  is the Lagrangian coordinates, and  $\Omega^0$  is the reference domain. For fixed  $\mathbf{X}$ ,  $\mathbf{x}(\mathbf{X}, t)$  describes the trajectory of a particle initially located at  $\mathbf{X}$ . For fixed  $t$ ,  $\mathbf{x}(\mathbf{X}, t)$  is a diffeomorphism between a reference domain  $\Omega^0$  to the current domain  $\Omega^t$ . In the current case, we have  $\Omega^t = \Omega$ . It is convenient to define the deformation tensor associated with the flow map  $\mathbf{x}(\mathbf{X}, t)$  in both Eulerian and Lagrangian coordinates by

$$\tilde{\mathbf{F}}(\mathbf{x}(\mathbf{X}, t), t) = \mathbf{F}(\mathbf{X}, t) = \nabla_{\mathbf{X}} \mathbf{x}(\mathbf{X}, t), \quad (11)$$

as the deformation tensor  $\mathbf{F}(\mathbf{X}, t)$  carries all the transport information of employed variables [48]. Here, the notation  $(\nabla_{\mathbf{X}} \mathbf{x}(\mathbf{X}, t))_{ij} = \frac{\partial x_i}{\partial X_j}$  is used. Applying the chain rule, one can show that in Eulerian coordinates,

the deformation tensor  $\tilde{\mathbf{F}}(\mathbf{x}, t)$  satisfies the transport equation [13]

$$\tilde{\mathbf{F}}_t + \mathbf{u} \cdot \nabla \tilde{\mathbf{F}} = (\nabla \mathbf{u}) \tilde{\mathbf{F}} , \quad (12)$$

where  $(\nabla \mathbf{u})_{ij} = u_{i,j} = \frac{\partial u_i}{\partial x_j}$ . For the incompressible fluid, we have

$$\rho(\mathbf{x}(\mathbf{X}, t), t) = \rho_0(\mathbf{X}), \quad \det \mathbf{F}(\mathbf{X}, t) = 1, \quad (13)$$

where  $\rho_0(\mathbf{X})$  is the initial density. Hence, the action  $\mathcal{A}[\mathbf{x}]$  can be written as

$$\mathcal{A}[\mathbf{x}(\mathbf{X}, t)] = \int_0^T \mathcal{K} - \mathcal{F} dt = \int_0^T \int_{\Omega^0} \rho_0(\mathbf{X}) |\mathbf{x}_t(\mathbf{X}, t)|^2 d\mathbf{X} dt , \quad (14)$$

in Lagrangian coordinates, which is a functional of the flow map  $\mathbf{x}(\mathbf{X}, t)$ . To compute the variable  $\mathcal{A}[\mathbf{x}]$  with respect to  $\mathbf{x}(\mathbf{X}, t)$ , we consider a perturbation  $\mathbf{x}^\epsilon(\mathbf{X}, t) = \mathbf{x}(\mathbf{X}, t) + \epsilon \mathbf{y}(\mathbf{X}, t)$ , where  $\mathbf{y}(\mathbf{X}, t) = \tilde{\mathbf{y}}(\mathbf{x}(\mathbf{X}, t), t)$  is the perturbation satisfying  $\tilde{\mathbf{y}} \cdot \mathbf{n} = 0$  with  $\mathbf{n}$  being the outer normal of  $\Omega$ . By direct computation, we have

$$\frac{d}{d\epsilon} \Big|_{\epsilon=0} \mathcal{A}[\mathbf{x}^\epsilon] = \int_0^T \int_{\Omega^0} \rho_0(\mathbf{X}) \mathbf{x}_t(\mathbf{X}, t) \cdot \mathbf{y}_t(\mathbf{X}, t) d\mathbf{X} dt = \int_0^T \int_{\Omega^0} -\rho_0(\mathbf{X}) \mathbf{x}_{tt}(\mathbf{X}, t) \cdot \mathbf{y}(\mathbf{X}, t) d\mathbf{X} dt , \quad (15)$$

where the second identity follows the integration by parts. Pushing forward to Eulerian coordinates, we have

$$\frac{d}{d\epsilon} \Big|_{\epsilon=0} \mathcal{A}[\mathbf{x}^\epsilon] = \int_0^T \int_{\Omega} -\rho(\mathbf{u}_t + \mathbf{u} \cdot \nabla \mathbf{u}) \cdot \tilde{\mathbf{y}} d\mathbf{x} dt , \quad (16)$$

which indicates

$$\frac{\delta \mathcal{A}}{\delta \mathbf{x}} = -\rho(\mathbf{u}_t + \mathbf{u} \cdot \nabla \mathbf{u}) \quad (17)$$

in Eulerian coordinates. For the dissipation part, we apply the MDP by considering a perturbation  $\mathbf{u}^\epsilon(\mathbf{x}, t) = \mathbf{u}(\mathbf{x}, t) + \epsilon \mathbf{v}(\mathbf{x}, t)$ . A direct computation shows that

$$\frac{d}{d\epsilon} \Big|_{\epsilon=0} \left( \int_{\Omega} \eta |\nabla \mathbf{u}^\epsilon|^2 - p(\nabla \cdot \mathbf{u}^\epsilon) d\mathbf{x} \right) = \int_{\Omega} (-\eta \Delta \mathbf{u} + \nabla p) \cdot \mathbf{v} d\mathbf{x} , \quad (18)$$

which indicates

$$\frac{\delta \mathcal{D}}{\delta \mathbf{x}_t} = \frac{\delta \mathcal{D}}{\delta \mathbf{u}} = -\eta \Delta \mathbf{u} + \nabla p . \quad (19)$$

Here,  $p$  is the Lagrangian multiplier for the incompressible condition  $\nabla \cdot \mathbf{u} = 0$ . Recall the force balance condition (6), we obtain the momentum equation in the incompressible Navier-Stokes equation (7) by combining (17) and (19).

## 2.2. EnVarA for the micro-macro model

As mentioned in the introduction, the well-used micro-macro model (1) employs an energy-dissipation law (4). More precisely, by a direct calculation, we can show the following result:

**Proposition 2.1.** *Suppose that  $(\mathbf{u}(\mathbf{x}, t), f(\mathbf{x}, \mathbf{q}, t))$  is a smooth solution of (1) satisfies the boundary conditions*

$$\mathbf{u}(\mathbf{x}, t) = 0, \quad f(\mathbf{x}, \mathbf{q}, t) = 0, \quad \mathbf{x} \in \partial\Omega, \quad \lim_{\|\mathbf{q}\| \rightarrow \infty} f(\mathbf{x}, \mathbf{q}, t) = 0,$$

*then  $(\mathbf{u}(\mathbf{x}, t), f(\mathbf{x}, \mathbf{q}, t))$  satisfies the following energy-dissipation law*

$$\frac{d}{dt} \int_{\Omega} \left( \frac{1}{2} \rho |\mathbf{u}|^2 + \lambda_p \int_{\mathbb{R}^d} k_B T f \ln f + \Psi f d\mathbf{q} \right) d\mathbf{x} = - \int_{\Omega} \left( \eta_s |\nabla \mathbf{u}|^2 + \int_{\mathbb{R}^d} \frac{\lambda_p \zeta}{2} f |\mathbf{V} - (\nabla \mathbf{u}) \mathbf{q}|^2 d\mathbf{q} \right) d\mathbf{x} \quad (20)$$

where

$$\mathbf{V}(\mathbf{x}, \mathbf{q}, t) = (\nabla \mathbf{u} \mathbf{q}) - \frac{2}{\zeta} \nabla_{\mathbf{q}} \Psi - \frac{2k_B T}{\zeta} \nabla_{\mathbf{q}} (\ln f) \quad (21)$$

is the microscopic velocity associated with the microscopic Fokker-Planck equation in (1).

*Proof.* We multiply the first equation of (1) by  $\mathbf{u}$  and integrate with respect to  $\mathbf{x}$  over domain  $\Omega$ . Using integration by parts and the fact that  $\mathbf{u}$  is divergence-free, we have

$$\frac{d}{dt} \int_{\Omega} \rho |\mathbf{u}|^2 d\mathbf{x} = - \int_{\Omega} \eta_s |\nabla \mathbf{u}|^2 d\mathbf{x} - \int_{\Omega} \boldsymbol{\tau} : \nabla \mathbf{u} d\mathbf{x}, \quad (22)$$

where  $A : B = \sum_{i,j} A_{ij} B_{ij}$ . Next, we multiply the third equation of (1) by  $k_B T \ln f + \Psi$  and integrate with respect to both  $\mathbf{q}$  over  $\mathbb{R}^d$  and  $\mathbf{x}$  over  $\Omega$ . Again, using integration by parts and the fact that  $\mathbf{u}$  is divergence-free, we can obtain

$$\frac{d}{dt} \int_{\Omega} \int_{\mathbb{R}^d} k_B T f \ln f + f \Psi d\mathbf{q} d\mathbf{x} = - \int_{\Omega} \int_{\mathbb{R}^d} \frac{2}{\zeta} f |\nabla_{\mathbf{q}} (k_B T \ln f + \Psi)|^2 + f (\nabla_{\mathbf{q}} \Psi \otimes \mathbf{q}) : \nabla \mathbf{u} d\mathbf{q} d\mathbf{x}. \quad (23)$$

Indeed, due to  $\nabla \cdot \mathbf{u} = 0$  and  $\nabla \Psi(\mathbf{q}) = 0$  (as  $\Psi$  doesn't depend on  $\mathbf{x}$ ), we have

$$\begin{aligned} & \int_{\Omega} \int_{\mathbb{R}^d} (\mathbf{u} \cdot \nabla f) (k_B T \ln f + \Psi) d\mathbf{q} d\mathbf{x} \\ &= \int_{\Omega} \int_{\mathbb{R}^d} -(\nabla \cdot \mathbf{u}) (k_B T f \ln f + f \Psi) - k_B T \mathbf{u} \cdot \nabla f d\mathbf{q} d\mathbf{x} = \int_{\Omega} \int_{\mathbb{R}^d} k_B T f (\nabla \cdot \mathbf{u}) d\mathbf{q} d\mathbf{x} = 0 \end{aligned} \quad (24)$$

and

$$\begin{aligned} & \int_{\Omega} \int_{\mathbb{R}^d} \nabla_{\mathbf{q}} \cdot ((\nabla \mathbf{u}) \mathbf{q} f) (k_B T \ln f) d\mathbf{q} d\mathbf{x} = \int_{\Omega} \int_{\mathbb{R}^d} -k_B T ((\nabla \mathbf{u}) \mathbf{q}) \cdot \nabla_{\mathbf{q}} f d\mathbf{q} d\mathbf{x} \\ &= \int_{\Omega} \int_{\mathbb{R}^d} k_B T \nabla_{\mathbf{q}} \cdot ((\nabla \mathbf{u}) \mathbf{q}) f d\mathbf{q} d\mathbf{x} = \int_{\Omega} \int_{\mathbb{R}^d} k_B T (\nabla \cdot \mathbf{u}) f d\mathbf{q} d\mathbf{x} = 0. \end{aligned} \quad (25)$$

Multiplying (23) by  $\lambda_p$  and adding it to (22), we obtain the energy-dissipation law (20).  $\square$

In what follows, we show that the micro-macro model (1) can be derived from the energy-dissipation law (20) along with the kinematics of the number density distribution function  $f(\mathbf{x}, \mathbf{q}, t)$ :

$$\partial_t f + \nabla \cdot (f \mathbf{u}) + \nabla_{\mathbf{q}} \cdot (f \mathbf{V}) = 0. \quad (26)$$

Here,  $\mathbf{u}(\mathbf{x}, t)$  is the macroscopic velocity, and  $\mathbf{V}(\mathbf{x}, \mathbf{q}, t)$  is microscopic velocity in the configuration space. The goal of EnVarA is to derive the equation of  $\mathbf{u}(\mathbf{x}, t)$  and  $\mathbf{V}(\mathbf{x}, \mathbf{q}, t)$  from (20) by combining LAP and MDP.

We first look at the dynamics at the microscopic, which is described by the microscopic energy-dissipation law

$$\frac{d}{dt} \mathcal{F}^{\text{micro}} = -2\mathcal{D}^{\text{micro}}, \quad \mathcal{F}^{\text{micro}} = \int_{\Omega} \int_{\mathbb{R}^d} k_B T f \ln f + \Psi f d\mathbf{q} d\mathbf{x}, \quad \mathcal{D}^{\text{micro}} = \frac{1}{2} \int_{\mathbb{R}^d} \frac{\zeta}{2} f |\mathbf{V} - (\nabla \mathbf{u}) \mathbf{q}|^2 d\mathbf{q}. \quad (27)$$

In the case that  $\mathbf{u} = 0$ , the microscopic energy-dissipation law (27) at each  $\mathbf{x}$  corresponds to the energy-dissipation law of a linear Fokker-Planck equation [49]. The micro-macro coupling is introduced through the relative friction between the microscopic velocity  $\mathbf{V}$  and the macroscopic induced velocity  $(\nabla \mathbf{u}) \mathbf{q}$ . It is assumed that the effects of macroscopic flow on the microscopic configuration include the linear transport of the center of mass and the stretching of the polymer chain, i.e.,  $\mathbf{q}(\mathbf{x}, \mathbf{Q}, t) = \tilde{\mathbf{F}}(\mathbf{x}, t) \mathbf{Q}$  [13]. This relation is the same as the Cauchy-Born rule in solid mechanics that relates the macroscopic deformation of crystals

to changes in lattice vectors [50]. Hence, the macroscopic-induced velocity can be computed as

$$\tilde{\mathbf{V}}(\mathbf{x}, \mathbf{q}, t) = \frac{d}{dt} \left( \tilde{\mathbf{F}} \mathbf{Q} \right) = \left( \frac{d}{dt} \tilde{\mathbf{F}} \right) \mathbf{Q} = (\tilde{\mathbf{F}}_t + \mathbf{u} \cdot \nabla \tilde{\mathbf{F}}) \mathbf{Q} = (\nabla \mathbf{u}) \tilde{\mathbf{F}} \mathbf{Q} = (\nabla \mathbf{u}) \mathbf{q},$$

where the transport equation of the deformation tensor (12) is used. To derive the microscopic dynamics, one can apply the EnVarA to the microscopic energy-dissipation law (27). Since the microscopic dynamics is a gradient flow with  $\mathcal{K}^{\text{mirco}} = 0$ , we only need to compute the variation of the microscopic free energy

$$\mathcal{F}^{\text{micro}}[\mathbf{q}] = \int_{\Omega} \int_{\mathbb{R}^d} k_B T f_0 \ln \left( \frac{f_0(\mathbf{x}, \mathbf{Q})}{\det G(\mathbf{x}, \mathbf{Q}, t)} \right) + \Psi(\mathbf{q}) f_0(\mathbf{x}, \mathbf{Q}) d\mathbf{Q} d\mathbf{x}, \quad (28)$$

with respect to the microscopic flow map  $\mathbf{q}(\mathbf{x}, \mathbf{Q}, t)$ . Here,  $f_0(\mathbf{x}, \mathbf{Q})$  is the initial density and  $G(\mathbf{x}, \mathbf{Q}, t) = \nabla_{\mathbf{Q}} \mathbf{q}(\mathbf{x}, \mathbf{Q}, t)$  is the microscopic deformation tensor. Similar to Eqs. (16) and (17), we take the variation of Eq. (28) with respect to  $\mathbf{q}$  in the microscopic Lagrangian coordinates, and push forward to microscopic Eulerian coordinates, we have

$$\frac{\delta \mathcal{F}^{\text{micro}}[\mathbf{q}]}{\delta \mathbf{q}} = f \nabla_{\mathbf{q}} (k_B T \ln f + \Psi). \quad (29)$$

For the dissipation part, by taking variation of

$$\mathcal{D}^{\text{micro}} = \frac{1}{2} \int_{\mathbb{R}^d} \frac{\zeta}{2} f |\mathbf{V} - (\nabla \mathbf{u}) \mathbf{q}|^2 d\mathbf{q},$$

we have  $\frac{\delta \mathcal{D}^{\text{micro}}}{\delta \mathbf{V}} = \frac{\zeta}{2} (\mathbf{V} - \nabla \mathbf{u} \mathbf{q})$ . By the force balance condition (6), we obtain

$$\frac{\zeta}{2} f (\mathbf{V} - \nabla \mathbf{u} \mathbf{q}) = -f \nabla_{\mathbf{q}} (k_B T \ln f + \Psi). \quad (30)$$

Combining Eq. (30) with Eq. (26), we get the equation on the microscopic scale:

$$f_t + \nabla \cdot (f \mathbf{u}) + \nabla_{\mathbf{q}} \cdot (\nabla \mathbf{u} \mathbf{q} f) = \frac{2}{\zeta} \nabla_{\mathbf{q}} \cdot (f \nabla_{\mathbf{q}} \Psi) + \frac{2k_B T}{\zeta} \Delta_{\mathbf{q}} f. \quad (31)$$

The variation procedure on the macro-level is similar to that in the simple fluid. When deriving the macroscopic force balance, to account for the ‘‘separation of scale’’, one should consider the microscopic configuration to be transported with the flow, which indicates that  $\mathbf{q} = \mathbf{F} \mathbf{Q}$  and  $\mathbf{V} = \tilde{\mathbf{V}} = (\nabla \mathbf{u}) \mathbf{q}$ . Hence, the action functional  $\mathcal{A}[\mathbf{x}]$  can be written as

$$\mathcal{A}[\mathbf{x}] = \int_0^T \int_{\Omega^0} \left[ \frac{1}{2} \rho |\mathbf{x}_t|^2 - \lambda_p \int_{\mathbb{R}^d} k_B T f_0 \ln f_0 + \Psi(\mathbf{F} \mathbf{Q}) f_0 d\mathbf{Q} \right] d\mathbf{X} dt \quad (32)$$

in Lagrangian coordinates. Here,  $f_0(\mathbf{X}, \mathbf{Q})$  is the initial number distribution function. Consider a perturbation  $\mathbf{x}^{\epsilon}(\mathbf{X}, t) = \mathbf{x}(\mathbf{X}, t) + \epsilon \mathbf{y}(\mathbf{X}, t)$ , where  $\mathbf{y}(\mathbf{X}, t) = \hat{\mathbf{y}}(\mathbf{x}(\mathbf{X}, t), t)$  is the perturbation satisfying  $\hat{\mathbf{y}} \cdot \mathbf{n} = 0$  with  $\mathbf{n}$  being the outer normal of  $\Omega$ . Then

$$\frac{d}{d\epsilon} \mathcal{A}(\mathbf{x}^{\epsilon}) \Big|_{\epsilon=0} = \int_0^T \int_{\Omega^0} \left[ -\rho \mathbf{x}_{tt} \cdot \mathbf{y} - \lambda_p \int_{\mathbb{R}^d} f_0 \nabla_{\mathbf{q}} \Psi \otimes \mathbf{Q} : \nabla_{\mathbf{X}} \mathbf{y} d\mathbf{Q} \right] d\mathbf{X} dt.$$

Pushing forward to Eulerian coordinates, we have

$$\begin{aligned}\frac{d}{d\epsilon}\mathcal{A}(\mathbf{x}^\epsilon)\Big|_{\epsilon=0} &= \int_0^T \int_\Omega \left[ -\rho(\mathbf{u}_t + \mathbf{u} \cdot \nabla \mathbf{u}) \cdot \tilde{\mathbf{y}} - \lambda_p \int_{\mathbb{R}^d} f \nabla_{\mathbf{q}} \Psi \otimes \mathbf{q} : \nabla_{\mathbf{x}} \tilde{\mathbf{y}} \right] dx dt \\ &= \int_0^T \int_\Omega \left( -\rho(\mathbf{u}_t + \mathbf{u} \cdot \nabla \mathbf{u}) + \lambda_p \nabla \cdot \left( \int_{\mathbb{R}^d} f \nabla_{\mathbf{q}} \Psi \otimes \mathbf{q} d\mathbf{q} \right) \right) \cdot \tilde{\mathbf{y}} dx dt.\end{aligned}$$

Hence, the LAP leads to

$$\frac{\delta \mathcal{A}}{\delta \mathbf{x}} = -\rho(\mathbf{u}_t + \mathbf{u} \cdot \nabla \mathbf{u}) + \lambda_p \nabla \cdot \left( \int_{\mathbb{R}^d} f \nabla_{\mathbf{q}} \Psi \otimes \mathbf{q} d\mathbf{q} \right) \quad (33)$$

in Eulerian coordinates. For the dissipation part, due to the “separation of scale”, the second term in the dissipation in (20) vanishes as  $\mathbf{V} = \tilde{\mathbf{V}}$  for the macroscopic dynamics. Hence, same to (19), we have  $\frac{\delta \mathcal{D}}{\delta \mathbf{x}_t} = -\eta_s \Delta \mathbf{u} + \nabla p$  by employing MDP. Here,  $p$  is the Lagrangian multiplier for the incompressible condition  $\nabla \cdot \mathbf{u} = 0$ . Hence, the macroscopic force balance results in the momentum equation

$$\rho(\mathbf{u}_t + \mathbf{u} \cdot \nabla \mathbf{u}) + \nabla p = \eta_s \Delta \mathbf{u} + \nabla \cdot \boldsymbol{\tau}, \quad (34)$$

where

$$\boldsymbol{\tau} = \lambda_p \int_{\mathbb{R}^d} f \nabla_{\mathbf{q}} \Psi \otimes \mathbf{q} d\mathbf{q} \quad (35)$$

is the induced stress from the configuration space, representing the microscopic contributions to the macroscopic level. Here,  $\otimes$  denotes a tensor product and  $\mathbf{u} \otimes \mathbf{v}$  is a matrix  $(u_i v_j)$  for two vectors  $\mathbf{u}$  and  $\mathbf{v}$ . The formula (35) is known as the Irving–Kirkwood formula or the Kramers’ expression for the induced stress [5].

### 2.3. Nondimensionalization of the micro-macro model

It is convenient to nondimensionalize the micro-macro model by introducing the following nondimensionalized parameters:

$$\text{Re} = \frac{\rho \tilde{U} \tilde{L}}{\eta}, \quad \text{Wi} = \frac{\lambda \tilde{U}}{\tilde{L}}, \quad \tilde{\eta}_s = \frac{\eta_s}{\eta}, \quad \epsilon_p = \frac{\eta_p}{\eta}, \quad \lambda = \frac{\zeta}{4H},$$

where  $\tilde{L} = \sqrt{\frac{k_B T}{H}}$  is the characteristic length scale,  $\tilde{U}$  is the characteristic velocity,  $\eta_p = \lambda_p k_B T \lambda$  is related to the polymer viscosity,  $\eta$  is the total fluid viscosity and  $\eta = \eta_s + \eta_p$ . The final nondimensionalized system reads as follows,

$$\begin{cases} \text{Re}(\mathbf{u}_t + \mathbf{u} \cdot \nabla \mathbf{u}) + \nabla p = \tilde{\eta}_s \Delta \mathbf{u} + \nabla \cdot \boldsymbol{\tau}, & \boldsymbol{\tau} = \frac{\epsilon_p}{\text{Wi}} \int f \nabla_{\mathbf{q}} \Psi \otimes \mathbf{q} d\mathbf{q}, \\ \nabla \cdot \mathbf{u} = 0, \\ f_t + \nabla \cdot (\mathbf{u} f) + \nabla_{\mathbf{q}} \cdot (\nabla \mathbf{u} \mathbf{q} f) = \frac{1}{2\text{Wi}} \nabla_{\mathbf{q}} \cdot (f \nabla_{\mathbf{q}} \Psi) + \frac{1}{2\text{Wi}} \Delta_{\mathbf{q}} f, \end{cases} \quad (36)$$

where

$$\Psi(\mathbf{q}) = \frac{1}{2} |\mathbf{q}|^2, \quad \nabla_{\mathbf{q}} \Psi = \mathbf{q},$$

in Hookean model, and

$$\Psi(\mathbf{q}) = -\frac{b}{2} \ln(1 - |\mathbf{q}|^2/b), \quad \nabla_{\mathbf{q}} \Psi = \frac{\mathbf{q}}{1 - |\mathbf{q}|^2/b}, \quad |\mathbf{q}| \leq b$$

with  $b = HQ_0^2/k_B T$  in FENE model.

### 3. The deterministic particle-FEM method

In this section, we construct the numerical scheme for the micro-macro model (1), which combines a finite element discretization of the macroscopic fluid dynamic equation [51, 52, 53] with a deterministic particle method for the microscopic Fokker-Planck equation [37]. To overcome the difficulty arising from micro-macro coupling, we first employ a discrete energetic variational approach to derive a particle-based micro-macro model. The discrete energetic variational approach follows the idea of “Approximation-then-Variation”, which first applies particle approximation to the continuous energy dissipation law. As an advantage, the derived coarse-grained system preserves the variational structure at the particle level.

#### 3.1. A coarse-grained particle-based model

For simplicity, we consider the spatially homogeneous case, and assume the number density function satisfies

$$\int_{\mathbb{R}^d} f(\mathbf{x}, \mathbf{q}, t) d\mathbf{q} = 1, \quad \forall \mathbf{x} \in \Omega, \quad (37)$$

Thus, for fixed  $\mathbf{x}$ ,  $f(\mathbf{x}, \mathbf{q}, t)$  can be approximated by

$$f(\mathbf{x}, \mathbf{q}, t) \approx f_N(\mathbf{x}, \mathbf{q}, t) = \sum_{i=1}^N \omega_i(\mathbf{x}, t) \delta(\mathbf{q} - \mathbf{q}_i(\mathbf{x}, t)), \quad \forall \mathbf{x} \in \Omega, \quad (38)$$

where  $N$  is the number of particles at  $\mathbf{x}$  and time  $t$ ,  $\{\mathbf{q}_i(\mathbf{x}, t)\}_{i=1}^N$  is a set of particles at  $\mathbf{x}$  and time  $t$ ,  $\omega_i(\mathbf{x}, t)$  is the weight of  $i$ -th particle. Due to (37), we have  $\sum_{i=1}^N \omega_i(\mathbf{x}, t) = 1$ . In the current work, we fix  $\omega_i(\mathbf{x}, t) = \frac{1}{N}$ .

**Remark 3.1.** *The spatial homogeneous assumption is valid if the initial condition  $f_0(\mathbf{x}, \mathbf{q})$  satisfies Eq. (37). Indeed, recall Fokker-Planck equation*

$$f_t + \nabla \cdot (f \mathbf{u}) + \nabla_{\mathbf{q}} \cdot (\nabla \mathbf{u} \mathbf{q} f) = \frac{2}{\zeta} \nabla_{\mathbf{q}} \cdot (f \nabla_{\mathbf{q}} \Psi) + \frac{2k_B T}{\zeta} \Delta_{\mathbf{q}} f. \quad (39)$$

Let  $n(\mathbf{x}, t) = \int_{\mathbb{R}^d} f(\mathbf{x}, \mathbf{q}, t) d\mathbf{q}$  be the number density of polymer chains. Integrating Eq. (39) with respect to  $\mathbf{q}$  and using the incompressible condition, Eq. (39) gives

$$\frac{\partial}{\partial t} n(\mathbf{x}, t) + \mathbf{u} \cdot \nabla_{\mathbf{x}} n(\mathbf{x}, t) = 0.$$

which indicates that  $n(\mathbf{x}(\mathbf{X}, t), t) = n_0(\mathbf{X})$  in Lagrangian coordinates. Hence,  $n_0(\mathbf{X}) = 1$  leads to  $n(\mathbf{x}, t) = 1$ .

**Remark 3.2.**  $\{\mathbf{q}_i(\mathbf{x}, t)\}_{i=1}^N$  can be viewed as representative particles that represent information of the number density distribution  $f(\mathbf{x}, \mathbf{q}, t)$  at  $\mathbf{x}$ . Since only  $\mathbf{q}_i(\mathbf{x}, t)$  needs to be computed at each time-step, the computational cost can be largely reduced, compared to computing  $f(\mathbf{x}, \mathbf{q}, t)$ .

In general, there are two approaches to developing deterministic particles method for the microscopic Fokker-Planck equation (39), known as “variation-then-discrete” [34] and “discrete-then-variation” approaches. In the first approach, recalling the definition of the microscopic velocity  $\mathbf{V}(\mathbf{x}, \mathbf{q}, t)$  in (21), we have

$$\dot{\mathbf{q}}_i \approx \mathbf{V}(\mathbf{x}, \mathbf{q}_i, t) = (\nabla \mathbf{u} \mathbf{q}_i) - \frac{2}{\zeta} \nabla_{\mathbf{q}} \Psi(\mathbf{q}_i) - \frac{2k_B T}{\zeta} \nabla_{\mathbf{q}} \ln f(\mathbf{q}_i). \quad (40)$$

The only difficulty in the above approximation is how to estimate  $\nabla_{\mathbf{q}} \ln f(\mathbf{q}_i)$  when  $f$  is replaced by the empirical measure  $f_N$ . One can replace the empirical measure  $f_N(\mathbf{q}) = \frac{1}{N} \sum_{j=1}^N \delta(\mathbf{q} - \mathbf{q}_j)$  by

$$f_N^h(\mathbf{q}) = \frac{1}{N} \sum_{j=1}^N K_h(\mathbf{q}, \mathbf{q}_j), \quad (41)$$

where  $K_h(\mathbf{q}, \mathbf{q}_j)$  is a smooth kernel function and  $h$  is the kernel bandwidth. A typical choice of  $K_h(\mathbf{q}, \mathbf{q}_j)$  is the Gaussian kernel, given by

$$K_h(\mathbf{q}, \mathbf{q}_j) = \frac{1}{(\sqrt{2\pi}h)^d} \exp\left(-\frac{|\mathbf{q} - \mathbf{q}_j|^2}{2h^2}\right),$$

where  $d$  is the dimension of the space. Consequently, we have

$$\nabla \ln f_N^h(\mathbf{q}) = \frac{\nabla f_N^h(\mathbf{q})}{f_N^h(\mathbf{q})} = \frac{\sum_{j=1}^N \nabla_{\mathbf{q}} K_h(\mathbf{q}, \mathbf{q}_j)}{\sum_{j=1}^N K_h(\mathbf{q}, \mathbf{q}_j)}, \quad (42)$$

which leads to the deterministic particle scheme [34]

$$\dot{\mathbf{q}}_i = (\nabla \mathbf{u}) \mathbf{q}_i - \frac{2}{\zeta} \nabla_{\mathbf{q}} \Psi(\mathbf{q}_i) - \frac{2k_B T}{\zeta} \frac{\sum_{j=1}^N \nabla_{\mathbf{q}_i} K_h(\mathbf{q}_i, \mathbf{q}_j)}{\sum_{j=1}^N K_h(\mathbf{q}_i, \mathbf{q}_j)} \quad (43)$$

However, as mentioned in [37], it is unclear whether (43) are gradient flows in the spatial homogeneous case ( $\nabla \mathbf{u} = 0$ ).

To maintain the variational structure in the particle level, we adopt the idea of “discrete-then-variation”, which first substitutes the approximation (38) into the microscopic energy-dissipation law (27). Following [36], the microscopic free energy  $\mathcal{F}^{\text{micro}}$  can be approximated by

$$\mathcal{F}_h^{\text{micro}} = \int_{\Omega} \lambda_p \int_{\mathbb{R}^d} k_B T f_N \ln f_N^h + \Psi f_N d\mathbf{q} d\mathbf{x} = \int_{\Omega} \frac{\lambda_p}{N} \sum_{i=1}^N \left[ k_B T \ln \left( \frac{1}{N} \sum_{j=1}^N K_h(\mathbf{q}_i, \mathbf{q}_j) \right) + \Psi(\mathbf{q}_i) \right] d\mathbf{x}. \quad (44)$$

and the microscopic dissipation potential  $\mathcal{D}^{\text{micro}}$  can be approximated by

$$\mathcal{D}_h^{\text{micro}} = \frac{1}{2} \int_{\Omega} \frac{\lambda_p \zeta}{2} \frac{1}{N} \sum_{i=1}^N |\dot{\mathbf{q}}_i - \nabla \mathbf{u} \mathbf{q}_i|^2 d\mathbf{x}, \quad (45)$$

where  $\dot{\mathbf{q}}_i = \partial_t \mathbf{q}_i + \mathbf{u} \cdot \nabla \mathbf{q}_i$  is the material derivative of  $\mathbf{q}_i$ ,  $(\nabla \mathbf{u}) \mathbf{q}_i$  is the particle velocity that is induced by the macroscopic flow as in the continuous model. Again, we use the kernel smoothing (41) to handle  $\ln f$  when  $f$  is replaced by the empirical measure  $f_N$ . The dynamics of  $\mathbf{q}_i(\mathbf{x}, t)$  can be derived by performing the EnVarA in terms of  $\mathbf{q}_i$  and  $\dot{\mathbf{q}}_i$ , i.e.,

$$\frac{\delta \mathcal{D}_h^{\text{micro}}}{\delta \dot{\mathbf{q}}_i} = -\frac{\delta \mathcal{F}_h^{\text{micro}}}{\delta \mathbf{q}_i},$$

which leads to

$$\dot{\mathbf{q}}_i = (\nabla \mathbf{u}) \mathbf{q}_i - \frac{2}{\zeta} \left[ k_B T \left( \frac{\sum_{j=1}^N \nabla_{\mathbf{q}_i} K_h(\mathbf{q}_i, \mathbf{q}_j)}{\sum_{j=1}^N K_h(\mathbf{q}_i, \mathbf{q}_j)} + \sum_{k=1}^N \frac{\nabla_{\mathbf{q}_i} K_h(\mathbf{q}_k, \mathbf{q}_i)}{\sum_{j=1}^N K_h(\mathbf{q}_k, \mathbf{q}_j)} \right) + \nabla_{\mathbf{q}_i} \Psi(\mathbf{q}_i) \right]. \quad (46)$$

Here,  $\dot{\mathbf{q}}_i = \partial_t \mathbf{q}_i + \mathbf{u} \cdot \nabla \mathbf{q}_i$ , and we denote  $K_h(\mathbf{q}_i - \mathbf{q}_j)$  by  $K_h(\mathbf{q}_i, \mathbf{q}_j)$  for convenience. As an advantage of the “Approximation-then-Variation” approach, it can be noticed that Eq. (46) is a gradient flow with respect to  $\mathbf{q}_i$  in the absence of the flow, i.e.  $\mathbf{u} = 0$  at  $\forall \mathbf{x}$ . Interestingly, (46) is identical to (43), except for an additional term. The additional term is important in maintaining the variational structure in the particle level.

The variational procedure for the macroscopic flow is almost the same as that in the continuous case, as

shown in Section 2. The final micro-macro system with particle approximation is given by

$$\begin{cases} \rho(\mathbf{u}_t + \mathbf{u} \cdot \nabla \mathbf{u}) + \nabla p = \eta_s \Delta \mathbf{u} + \nabla \cdot \boldsymbol{\tau}, & \boldsymbol{\tau}(\mathbf{x}, t) = \lambda_p \frac{1}{N} \sum_{i=1}^N \nabla_{\mathbf{q}} \Psi(\mathbf{q}_i(\mathbf{x}, t)) \otimes \mathbf{q}_i(\mathbf{x}, t), \\ \nabla \cdot \mathbf{u} = 0, \end{cases} \quad (47)$$

where  $\mathbf{q}_i(\mathbf{x}, t)$  satisfies Eq. (46). One can view the macroscopic flow equation (47) along with the microscopic evolution equation (46) as a coarse-grained model for the original micro-macro model (1). As an advantage of the energetic variational approach, one can show that the coarse-grained model (46)-(47) satisfies the energy-dissipation law

$$\frac{d}{dt} \int_{\Omega} \rho |\mathbf{u}|^2 + \frac{\lambda_p}{N} \sum_{i=1}^N \left[ k_B T \ln \left( \frac{1}{N} \sum_{j=1}^N K_h(\mathbf{q}_i - \mathbf{q}_j) \right) + \Psi(\mathbf{q}_i) \right] d\mathbf{x} = - \int_{\Omega} \eta_s |\nabla \mathbf{u}|^2 + \frac{\lambda_p \zeta}{2} \frac{1}{N} \sum_{i=1}^N |\dot{\mathbf{q}}_i - \nabla \mathbf{u} \mathbf{q}_i|^2 d\mathbf{x}. \quad (48)$$

In other word, the deterministic particle approximation maintains the variational structure of the continuous system, which is crucial in establishing the well-posedness of the coarse-grained model and proving the convergence for  $N \rightarrow \infty$ .

The coarse-grained model (46)-(47) can be non-dimensionalized by using the same nondimensionalized parameters as in the continuous case. The final nondimensionalized system reads

$$\begin{cases} \text{Re}(\mathbf{u}_t + \mathbf{u} \cdot \nabla \mathbf{u}) + \nabla p = \tilde{\eta}_s \Delta \mathbf{u} + \nabla \cdot \boldsymbol{\tau}, & \boldsymbol{\tau} = \frac{\epsilon_p}{\text{Wi}} \frac{1}{N} \sum_{i=1}^N \nabla_{\mathbf{q}} \Psi(\mathbf{q}_i(\mathbf{x}, t)) \otimes \mathbf{q}_i(\mathbf{x}, t), \\ \nabla \cdot \mathbf{u} = 0, \end{cases} \quad (49)$$

with  $\mathbf{q}_i(\mathbf{x}, t)$  satisfying

$$\partial_t \mathbf{q}_i + \mathbf{u} \cdot \nabla \mathbf{q}_i - (\nabla \mathbf{u}) \mathbf{q}_i = -\frac{1}{2 \text{Wi}} \left( \frac{\sum_{j=1}^N \nabla_{\mathbf{q}_i} K_h(\mathbf{q}_i, \mathbf{q}_j)}{\sum_{j=1}^N K_h(\mathbf{q}_i, \mathbf{q}_j)} + \sum_{k=1}^N \frac{\nabla_{\mathbf{q}_i} K_h(\mathbf{q}_k, \mathbf{q}_i)}{\sum_{j=1}^N K_h(\mathbf{q}_k, \mathbf{q}_j)} + \nabla_{\mathbf{q}_i} \Psi(\mathbf{q}_i) \right). \quad (50)$$

Due to the presence of the convection term  $\mathbf{u} \cdot \nabla \mathbf{q}_i(\mathbf{x}, t)$ ,  $\mathbf{q}_i(\mathbf{x}, t)$  should be viewed as a field rather than a particle at  $\mathbf{x}$ . However, introducing a spatial discretization might significantly increase the computational cost. To overcome this difficulty, we will adopt a Lagrangian approach to deal with the convection term, which leads to an independent ensemble of particles in each  $\mathbf{x}$  when  $\mathbf{u} \cdot \nabla \mathbf{q}_i(\mathbf{x}, t) \neq 0$ .

**Remark 3.3.** *A key step in the above deterministic particle scheme is to replace the empirical measure  $f_N$  by  $f_N^h$  using kernel smoothing (41) when computing  $\ln f$  in the free energy. The choice of kernel bandwidth  $h$  is important for the accuracy and robustness of the numerical scheme below. Intuitively, if  $h$  is too small, then  $f_N^h$  will be oscillated. Consequently, it fails to provide a good approximation to  $\ln f$  and  $\nabla(\ln f)$ , and the term  $\frac{\sum_{j=1}^N \nabla_{\mathbf{q}_i} K_h(\mathbf{q}_i, \mathbf{q}_j)}{\sum_{j=1}^N K_h(\mathbf{q}_i, \mathbf{q}_j)} + \sum_{k=1}^N \frac{\nabla_{\mathbf{q}_i} K_h(\mathbf{q}_k, \mathbf{q}_i)}{\sum_{j=1}^N K_h(\mathbf{q}_k, \mathbf{q}_j)}$  will be very large. On the other hand, if  $h$  is too large,  $f_N^h$  will be flatten and the term  $\frac{\sum_{j=1}^N \nabla_{\mathbf{q}_i} K_h(\mathbf{q}_i, \mathbf{q}_j)}{\sum_{j=1}^N K_h(\mathbf{q}_i, \mathbf{q}_j)} + \sum_{k=1}^N \frac{\nabla_{\mathbf{q}_i} K_h(\mathbf{q}_k, \mathbf{q}_i)}{\sum_{j=1}^N K_h(\mathbf{q}_k, \mathbf{q}_j)}$  will be almost zero, which also fails to approximate  $\nabla \ln f_N^h$ . The optimal kernel bandwidth depends on the potential  $\Psi(\mathbf{q})$  and the macroscopic flow. In the current study, we choose the kernel bandwidth  $h$  through multiple numerical experiments (see the numerical sections for details).*

### 3.2. Full discrete scheme

In this subsection, we construct a full discrete scheme for the coarse-grained model (Eqs. (49) and (50)). To solve the micro-macro system numerically, it is a natural idea to develop some decoupled schemes. Precisely, we propose the following scheme for the temporal discretization:

- Step 1: Treat the viscoelastic stress  $\boldsymbol{\tau}^n$  explicitly, and solve the equation (49) to obtain updated values for the velocity and pressure.
- Step 2: Use the updated velocity field  $\mathbf{u}^{n+1}$  to solve the equation of  $\mathbf{q}_i$  at each node, and then update values of the viscoelastic stress, denoted by  $\boldsymbol{\tau}^{n+1}$ .

Eq. (49) in the first step can be solved by a standard incremental pressure-correction scheme [54] reads as follows:

- Step 1.1:

$$\operatorname{Re}\left(\frac{\tilde{\mathbf{u}}^{n+1} - \mathbf{u}^n}{\Delta t} + \mathbf{u}^n \cdot \nabla \tilde{\mathbf{u}}^{n+1}\right) + \nabla p^n = \tilde{\eta}_s \Delta \tilde{\mathbf{u}}^{n+1} + \nabla \cdot \boldsymbol{\tau}^n, \quad (51)$$

- Step 1.2:

$$\begin{cases} \frac{\mathbf{u}^{n+1} - \tilde{\mathbf{u}}^{n+1}}{\Delta t} + \nabla(p^{n+1} - p^n) = 0, \\ \nabla \cdot \mathbf{u}^{n+1} = 0. \end{cases} \quad (52)$$

We use the finite element method developed in Refs. [52, 53] for spatial discretization, employing the inf-sup stable Iso-P2/P1 element [55, 56] for velocity and pressure, and a linear element for each stress component. More precisely, let  $\Omega$  be the bounded computational domain,  $\mathcal{T}_h$  and  $\hat{\mathcal{T}}_h$  be two triangulations of  $\Omega$ , with  $\mathcal{T}_h$  being the uniform refinement of  $\hat{\mathcal{T}}_h$ . We denote  $\mathcal{T}_h$  and  $\hat{\mathcal{T}}_h$  as sets of simplexes  $\{\kappa_e | e = 1, \dots, M\}$  and  $\{\hat{\kappa}_e | e = 1, \dots, \hat{M}\}$ , respectively.  $N_h = \{\mathbf{x}_1, \dots, \mathbf{x}_{N_x}\}$  and  $\hat{N}_h = \{\hat{\mathbf{x}}_1, \dots, \hat{\mathbf{x}}_{\hat{N}_x}\}$  are sets of nodal points. We construct the finite-dimensional subspaces  $S_h$ ,  $\hat{S}_h \subset H^1(\Omega)$  and  $S_h^0 \subset H_0^1(\Omega)$  as follows:

$$S_h = \{g \in C^0(\bar{\Omega}) : g|_\kappa \in P_1(\kappa)\}, \quad \hat{S}_h = \{g \in C^0(\bar{\Omega}) : g|_{\hat{\kappa}} \in P_1(\hat{\kappa})\}, \quad S_h^0 = \{g \in S_h : g|_{\partial\Omega} = 0\},$$

where  $P_r(\kappa)$  is the space of polynomial functions of degree less than or equal to  $r$  on the simplex  $\kappa$ . We let  $V_\tau = (S_h)^{d^2}$  with  $d$  the dimension of space,  $V_{\mathbf{u}_h} = (S_h^0)^d$  and  $M_h = \hat{S}_h \cap L_0^2(\Omega)$ . One can show that  $V_{\mathbf{u}_h}$  and  $M_h$  satisfy the inf-sup condition [57, 55]

$$\inf_{p_h \in M_h} \sup_{\mathbf{u}_h \in V_{\mathbf{u}_h}} \frac{\int_\Omega p_h \nabla \cdot \mathbf{u}_h d\mathbf{x}}{\|p_h\| \|\mathbf{u}_h\|_1} \geq C,$$

where  $C > 0$  is independent of mesh size  $h$  and  $\|\mathbf{u}_h\|_1 = \|\nabla \mathbf{u}_h\| + \|\mathbf{u}_h\|$ .

The full discretization scheme for Step 1 can be summarized as follows. Given  $\mathbf{u}_h^n \in V_{\mathbf{u}_h}$ ,  $\boldsymbol{\tau}_h^n \in V_\tau$  and  $p_h^n \in M_h$  for  $n > 0$ , we compute  $\mathbf{u}_h^{n+1}$  and  $p_h^{n+1}$  by the following algorithm:

- Step 1.1: Find  $\tilde{\mathbf{u}}_h^{n+1} \in V_{\mathbf{u}_h}$ , such that for any  $\mathbf{v} \in V_{\mathbf{u}_h}$ ,

$$\operatorname{Re}\left(\frac{1}{\Delta t} \tilde{\mathbf{u}}_h^{n+1} + \mathbf{u}_h^n \cdot \nabla \tilde{\mathbf{u}}_h^{n+1}, \mathbf{v}\right) + (\tilde{\eta}_s \nabla \tilde{\mathbf{u}}_h^{n+1}, \nabla \mathbf{v}) = \operatorname{Re}\left(\frac{1}{\Delta t} \mathbf{u}_h^n, \mathbf{v}\right) - (\nabla p_h^n, \mathbf{v}) + (\nabla \cdot \boldsymbol{\tau}_h^n, \mathbf{v}).$$

- Step 1.2: Find  $p_h^{n+1} \in M_h$ , such that for any  $\psi \in M_h$ ,

$$(\nabla(p_h^{n+1} - p_h^n), \nabla \psi) = -\frac{1}{\Delta t} (\nabla \cdot \tilde{\mathbf{u}}_h^{n+1}, \psi).$$

and update  $\mathbf{u}_h^{n+1}$  by

$$\mathbf{u}_h^{n+1} = \tilde{\mathbf{u}}_h^{n+1} - \Delta t \nabla(p_h^{n+1} - p_h^n).$$

**Remark 3.4.** In Step 1, the pressure-correction scheme has been adopted to decouple velocity  $\mathbf{u}^{n+1}$  and pressure  $p^{n+1}$  in Eq. (49). Although the pressure-correction scheme can lead to an invertible discrete linear

system at each time step regardless of whether the inf-sup condition is satisfied, the inf-sup condition is crucial for the stability and convergence of the numerical scheme [54]. Hence, in the current study, the inf-sup stable Iso-P2/P1 element is adopted.

Next we discuss how to solve microscopic part (46) with a given  $\mathbf{u}_h^{n+1}$  at each node  $\mathbf{x}_\alpha$ . One difficulty is that  $\mathbf{q}_i$  is a function of  $\mathbf{x}$  and  $t$  due to the convection term  $\mathbf{u} \cdot \nabla \mathbf{q}_i(\mathbf{x}, t)$ . Many earlier numerical studies based on CONNFFESSIT algorithms either focus on the shear flows in which the convection term vanishes or ignores the convection term [58, 19]. To deal with the convection term in stochastic methods, two types of methods have been developed. One is to introduce a spatial-temporal discretization to  $\mathbf{q}_i$ , as used in Brownian Configuration Field method [59, 60, 25]. Another way is to use a Lagrangian viewpoint to compute the convection term [15]. In the current study, we use the idea of the second approach, and use an operator splitting approach to solve Eq. (46). Initially, we assign ensemble of particles  $\{\mathbf{q}_{\alpha,i}\}_{i=1}^N$  to each node  $\mathbf{x}_\alpha$  ( $\alpha = 1, 2, \dots, N_x$ ). We assume that  $f(\mathbf{x}, \mathbf{q}, 0)$  is spatially homogeneous, and use the same ensemble of initial samples at all  $\mathbf{x}_\alpha$ . Within the values  $\mathbf{u}_h^{n+1}$ , we solve the microscopic equation (46) by the following two steps:

- Step 2.1: At each node  $\mathbf{x}_\alpha$ , solve Eq. (50) without the convection term  $\mathbf{u}_h^{n+1} \cdot \nabla \mathbf{q}_i$  by

$$\begin{aligned} \frac{1}{N} \frac{\mathbf{q}_i^{n+1,*} - \mathbf{q}_i^n}{\Delta t} &= -\frac{1}{2\text{Wi}} \frac{\delta \hat{\mathcal{F}}_h}{\delta \mathbf{q}_i} (\{\mathbf{q}_i^{n+1,*}\}_{i=1}^N), \\ \mathbf{q}^{n+1,**} &= (\mathbf{I} + (\nabla \mathbf{u}_h^{n+1}) \Delta t) \mathbf{q}^{n+1,*}. \end{aligned} \quad (53)$$

where  $\hat{\mathcal{F}}_h[\{\mathbf{q}_i\}_{i=1}^N] = \frac{1}{N} \sum_{i=1}^N \left[ \ln \left( \frac{1}{N} \sum_{j=1}^N K_h(\mathbf{q}_i - \mathbf{q}_j) \right) + \Psi(\mathbf{q}_i) \right]$  is the non-dimensionalized discrete microscopic free energy at each node. We omit the index  $\alpha$  when it does not cause confusion.

- Step 2.2: To deal with the convection term  $\mathbf{u} \cdot \mathbf{q}_i$ , we view each node  $\mathbf{x}_\alpha$  as a Lagrangian particle, and update it according to the Eulerian velocity field  $\mathbf{u}_h^{n+1}$  at each node

$$\tilde{\mathbf{x}}_\alpha = \mathbf{x}_\alpha + \Delta t (\mathbf{u}_h^{n+1}|_{\mathbf{x}_\alpha}), \quad \alpha = 1, 2, \dots, N_x. \quad (54)$$

Hence,  $\{\mathbf{q}_{\alpha,i}^{n+1,**}\}$  is an ensemble of samples at the new point  $\tilde{\mathbf{x}}_\alpha$ . To obtain  $\mathbf{q}_{\alpha,i}^{n+1}$  at  $\mathbf{x}_\alpha$ , we use a linear interpolation to get  $\mathbf{q}_{\alpha,i}^{n+1}$  (at mesh with  $\{\mathbf{x}_\alpha\}$  being the set of nodes) from  $\mathbf{q}_{\alpha,i}^{n+1,**}$  (at mesh with  $\{\tilde{\mathbf{x}}_\alpha\}$  being nodes) for each  $i$ .

An advantage of the above update-and-projection approach is that it doesn't require a spatial discretization on  $\mathbf{q}_i(\mathbf{x}, t)$ . Within the ensemble of particles  $\{\mathbf{q}_{\alpha,i}^{n+1}\}_{i=1}^N$  on each node  $\mathbf{x}_\alpha$ , the updated values of the viscoelastic stress  $\tau_h^{n+1}$  at each node, denoted as  $\{\tau_\alpha^{n+1}\}_{\alpha=1}^{N_x}$ , can be obtained through the second equation of Eq. (49). And then project them into the finite element space of  $\boldsymbol{\tau}$ , i.e.  $V_{\boldsymbol{\tau}}$ . To this end, we choose the projection operator  $\mathcal{I}$ , such that, for each component of the stress  $\tau_{\alpha,l,k}^{n+1}$  with  $l, k = 1, \dots, d$ ,  $\mathcal{I}(\{\tau_{\alpha,l,k}^{n+1}\}_{\alpha=1}^{N_x}) := \sum_{\alpha=1}^{N_x} \tau_{\alpha,l,k}^{n+1} \phi_\alpha$ , where  $\{\phi_\alpha : \alpha = 1, \dots, N_x\} \subset S_h$  denotes the nodal basis for  $S_h$ .

**Remark 3.5.** The operator splitting approach has been widely used in many previous Fokker-Planck based numerical approaches for micro-macro models [61]. One important reason is that the system admits a variational structure without the convection terms. Moreover, by separating the convection component, the particles at each physical location can be treated independently, which largely saves the computational cost.

Since the first step in (53) admits a variational structure, the implicit Euler discretization can be reformulated as an optimization problem. In more detail, at each node  $\mathbf{x}_\alpha$ , we define

$$J_n[\{\mathbf{q}_i\}_{i=1}^N] = \frac{1}{N} \sum_{i=1}^N \left( \frac{1}{2\Delta t} |\mathbf{q}_i - \mathbf{q}_i^n|^2 \right) + \frac{1}{2\text{Wi}} \hat{\mathcal{F}}_h[\{\mathbf{q}_i\}_{i=1}^N],$$

where  $\hat{\mathcal{F}}_h[\{\mathbf{q}_i\}_{i=1}^N] = \frac{1}{N} \sum_{i=1}^N \left[ \ln \left( \frac{1}{N} \sum_{j=1}^N K_h(\mathbf{q}_i - \mathbf{q}_j) \right) + \Psi(\mathbf{q}_i) \right]$ . We can obtain a solution to the nonlinear system by solving an optimization problem [37, 62]

$$\{\mathbf{q}_i^{n+1,*}\}_{i=1}^N = \arg \min_{\{\mathbf{q}_i\}_{i=1}^N} J_n(\{\mathbf{q}_i\}_{i=1}^N). \quad (55)$$

An advantage of this reformulation is that we can prove the existence of the  $\mathbf{q}_i^{n+1,*}$ . More precisely, we have the following result.

**Proposition 3.1.** *For any given  $\{\mathbf{q}_i^n\}_{i=1}^N$  at  $\mathbf{x}_\alpha$ , there exists at least one minimal solution  $\{\mathbf{q}_i^{n+1}\}_{i=1}^N$  of (55) that also satisfies*

$$\frac{1}{2\text{Wi}} \frac{\hat{\mathcal{F}}_h(\{\mathbf{q}_i^{n+1}\}_{i=1}^N) - \hat{\mathcal{F}}_h(\{\mathbf{q}_i^n\}_{i=1}^N)}{\Delta t} \leq -\frac{1}{2N\Delta t^2} \sum_{i=1}^N |\mathbf{q}_i^{n+1} - \mathbf{q}_i^n|^2. \quad (56)$$

*Proof.* Let  $\mathbf{X} \in \mathbb{R}^D$  ( $D = N \times d$ ) be vectorized  $\{\mathbf{q}_i\}_{i=1}^N$ , namely,

$$\mathbf{X} = (q_{1,1}, \dots, q_{N,1}, q_{1,2}, \dots, q_{N,2}, \dots, q_{N,d}).$$

Denote  $\hat{\mathcal{F}}_h(\{\mathbf{q}_i\}_{i=1}^N)$  and  $J_n(\{\mathbf{q}_i\}_{i=1}^N)$  as  $\hat{\mathcal{F}}_h(\mathbf{X})$  and  $J_n(\mathbf{X})$  respectively. For given  $\mathbf{X}^n = \{\mathbf{q}_i^n\}_{i=1}^N$ , we define

$$S = \{J_n(\mathbf{X}) \leq J_n(\mathbf{X}^n)\}$$

be the admissible set. Obviously,  $S$  is non-empty and closed, since  $\mathbf{X}^n \in S$  and  $J_n(\mathbf{X})$  is continuous. Moreover, it's easy to prove that  $\hat{\mathcal{F}}_h(\mathbf{X})$  is bounded from below, since

$$\ln \left( \frac{1}{N} \sum_{j=1}^N K_h(\mathbf{q}_i^n, \mathbf{q}_j^n) \right) \geq \ln \left( \frac{1}{N} \frac{1}{(\sqrt{2\pi h})^d} \right) \quad \text{and} \quad \Psi(\mathbf{q}_i) \geq 0.$$

And thus,  $J_n(\mathbf{X})$  is coercive and  $S$  is a bounded set. Hence,  $J_n(\mathbf{X})$  admits a global minimizer  $\mathbf{X}^{n+1}$  in  $S$ . And thus, we have

$$\frac{1}{N} \sum_{i=1}^N \left( \frac{1}{2\Delta t} |\mathbf{q}_i^{n+1} - \mathbf{q}_i^n|^2 \right) + \frac{1}{2\text{Wi}} \hat{\mathcal{F}}_h(\mathbf{X}^{n+1}) \leq \frac{1}{2\text{Wi}} \hat{\mathcal{F}}_h(\mathbf{X}^n), \quad (57)$$

which is equivalent to Eq. (56).  $\square$

In the numerical implementation, we adopt the Barzilai-Borwein gradient method [63] to solve the optimization problem (55). The Barzilai-Borwein method is a gradient descent algorithm with an adaptive stepsize, which updates  $\mathbf{X}^k$  (vectorized  $\{\mathbf{q}_i\}_{i=1}^N$ ) through

$$\mathbf{X}^k = \mathbf{X}^{k-1} - \alpha_{k-1} \nabla_{\mathbf{X}} J_n(\mathbf{X}^{k-1}) \quad (58)$$

where  $\alpha_{k-1} = \mathbf{s}_k^T \mathbf{s}_k / (\mathbf{s}_k^T \mathbf{y}_k)$  is a BB stepsize. Here,  $\mathbf{y}_k = \nabla_{\mathbf{X}} J(\mathbf{X}^{k-1}) - \nabla_{\mathbf{X}} J(\mathbf{X}^{k-2})$  and  $\mathbf{s}_k = \mathbf{X}^{k-1} - \mathbf{X}^{k-2}$ . We compute  $\mathbf{X}^1$  by using gradient descent with stepsize  $10^{-7}$ . The initial guess,  $\mathbf{X}^0$ , is taken as vectorized  $\{\mathbf{q}_i^n\}_{i=1}^N$ . The stopping criteria are set to  $\|\nabla_{\mathbf{X}} J(\mathbf{X})\|_2 \leq 10^{-9}$  or reaching the maximum number of inner iterations, which is set to 50.

**Remark 3.6.** *In the current numerical scheme, we estimate the macroscopic stress tensor by taking microscopic distribution function as the empirical measure for the finite number of particles  $\{\mathbf{q}_i\}_{i=1}^N$ . More advanced techniques can be applied to this stage to obtain a more accurate estimation to the stress tensor, such as the maximum-entropy based algorithm developed in Ref. [64] and Ref. [65] that reconstructs basis functions from particles. We'll explore this perspective in future works.*

## 4. Results and discussion

In this section, we perform various numerical experiments to validate the proposed numerical scheme by studying various well-known benchmark problems for the micro-macro models [17, 19, 41].

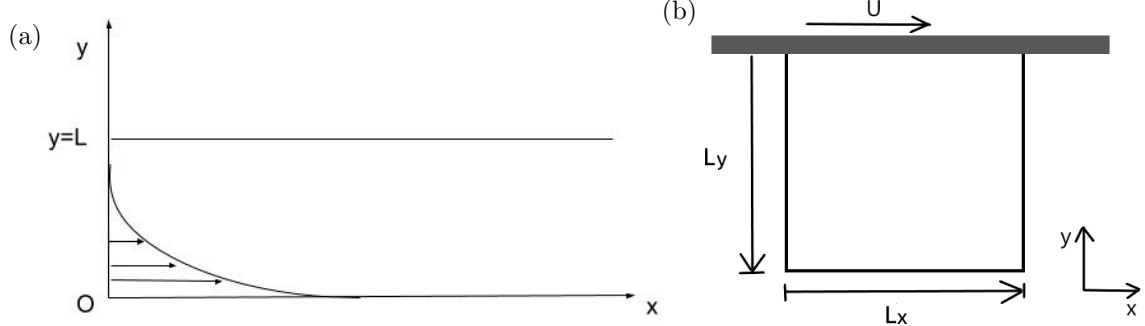


**Figure 1:** Schematic representation of (a) the initial simple shear flow and (b) the lid-driven cavity flow.

We consider two flow scenarios: a simple shear flow and a lid-driven cavity flow. In a simple shear flow, a viscous fluid is enclosed between two parallel planes of infinite length, separated by a distance  $L$ , see Figure 1(a) for an illustration. At  $t = 0$ , the lower plane moves in the positive  $x$  direction with a constant velocity  $U$ . Due to the special geometry of simple shear flows, it is common to use the ansatz  $\mathbf{u}(\mathbf{x}, t) = (u(y, t), 0)$ , which means the velocity field  $\mathbf{u}(\mathbf{x}, t)$  is in the  $x$ -direction and depends only on the  $y$ -variable only. Additionally, we use the ansatz that  $\mathbf{q}_i$  depends only on  $y$ -variable, which implies that  $\mathbf{u} \cdot \nabla \mathbf{q}_i = 0$  [6, 17]. Hence, the micro-macro model can be simplified into:

$$\left\{ \begin{array}{l} \text{Re} \frac{\partial u}{\partial t}(y, t) = \tilde{\eta}_s \frac{\partial^2 u}{\partial y^2}(y, t) + \frac{\partial \tau_{21}}{\partial y}(y, t), \\ \tau_{21} = \frac{\epsilon_p}{\text{Wi}} \frac{1}{N} \sum_{i=1}^N [\nabla_{\mathbf{q}} \Psi(\mathbf{q}_i)]_1 q_{i2}(y, t), \\ \frac{\partial q_{i1}}{\partial t}(y, t) - \frac{\partial u}{\partial y} q_{i2}(y, t) = -\frac{1}{2\text{Wi}} \left( \left[ \frac{\sum_{j=1}^N [\nabla_{\mathbf{q}_i} K_h(\mathbf{q}_i, \mathbf{q}_j)]_1}{\sum_{j=1}^N K_h(\mathbf{q}_i, \mathbf{q}_j)} + \sum_{k=1}^N \frac{[\nabla_{\mathbf{q}_i} K_h(\mathbf{q}_k, \mathbf{q}_i)]_1}{\sum_{j=1}^N K_h(\mathbf{q}_k, \mathbf{q}_j)} \right] + [\nabla_{\mathbf{q}_i} \Psi(\mathbf{q}_i)]_1 \right), \\ \frac{\partial q_{i2}}{\partial t}(y, t) = -\frac{1}{2\text{Wi}} \left( \left[ \frac{\sum_{j=1}^N [\nabla_{\mathbf{q}_i} K_h(\mathbf{q}_i, \mathbf{q}_j)]_2}{\sum_{j=1}^N K_h(\mathbf{q}_i, \mathbf{q}_j)} + \sum_{k=1}^N \frac{[\nabla_{\mathbf{q}_i} K_h(\mathbf{q}_k, \mathbf{q}_i)]_2}{\sum_{j=1}^N K_h(\mathbf{q}_k, \mathbf{q}_j)} \right] + [\nabla_{\mathbf{q}_i} \Psi(\mathbf{q}_i)]_2 \right), \end{array} \right. \quad (59)$$

where  $\tau_{21}$  is the off-diagonal component of the extra-stress tensor  $\boldsymbol{\tau}$ ,  $\mathbf{q}_i = (q_{i1}, q_{i2})$  and  $[\mathbf{g}]_l$  denotes the  $l$ th component of the vector  $\mathbf{g}$  ( $l = 1, 2$ ).

In the lid-driven cavity flow, the polymeric fluid is bounded in a two-dimensional rectangular box of width  $L_x$  and height  $L_y$ , and the fluid motion is induced by the translation of the upper wall at a velocity  $U$ . The width of the cavity is set to be  $L_x = 1$ , and the horizontal velocity of the lid  $u(x) = U = 1$ . The three other walls are stationary, and the boundary conditions applied to them are non-slip and impermeable (see Fig. 1(b)). In this case, a full 2D Navier-Stokes equation needs to be solved.

For all the numerical experiments carried out in this section, we assume that the flow is two-dimensional and the dumbbells lie in the plane of the flow, namely, the configuration vector  $\mathbf{q}$  is also two-dimensional. At each node, we use the same initial ensemble of  $N$  particles, sampled from the 2-dimensional standard normal distribution.

### 4.1. Hookean model: simple shear flow

It is well known that the micro-macro model (1) with a Hookean potential  $\Psi(\mathbf{q}) = \frac{1}{2}H|\mathbf{q}|^2$  is equivalent to a macroscopic viscoelastic model, the Oldroyd-B model. For the Oldroyd-B model, an analytical solution

for the start-up of plane Couette flow in a 2D channel is available (see [17, 25]). So we can test the accuracy of the proposed numerical scheme by comparing the simulation results of the micro-macro model with the analytical solutions of the corresponding Oldroyd-B model.

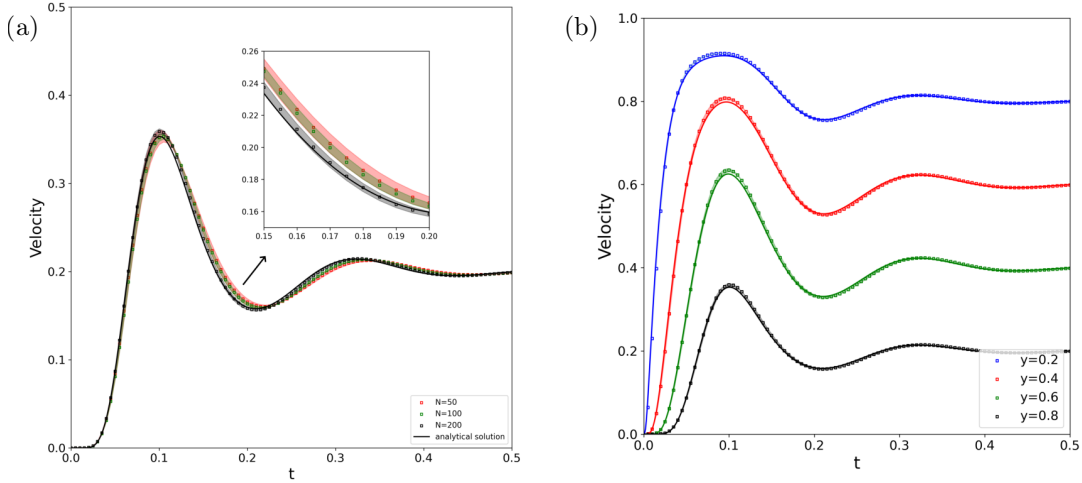


**Figure 2:** (a). Time evolution of velocity at  $y = 0.8$  with different numbers of particles. The analytical solution of the corresponding Oldroyd-B model is shown in a black line. (b), Comparison of the velocity of the Hookean case with particle number  $N = 200$  (marker) and the analytical solution (solid line) at different times and different locations ( $y = 0.2, 0.4, 0.6, 0.8$ ).

We choose the physical parameters as follows:  $Re = 0.11$ ,  $Wi = 0.1$ ,  $\tilde{\eta}_s = 0.11$  and  $\epsilon_p = 0.89$ . The number of elements is  $M = 40$  and the time step is  $\Delta t = 10^{-3}$ . Additionally, we choose the kernel bandwidth as  $h^2 = \text{med}_n^2 / \log N$  using the median trick proposed in [66] to compute  $\{\mathbf{q}^{n+1}\}_{i=1}^N$ . Here,  $\text{med}_n$  denotes the median of the pairwise distances between the particles  $\{\mathbf{q}_i^n\}_{i=1}^N$ .

We begin by examining the impact of the number of particles on numerical results. Figure 2(a) shows the time evolution of velocity at  $y = 0.8$  for different numbers of particles ( $N = 50, 100, 200$ ). we perform 10 independent runs, where we use the same parameters and different sets of initial particles. Each marker on the plot represents the mean values, indicating mean values  $\pm$  standard errors [6]. The results show that as the number of particles increases, the mean values converge to the analytical solution and the standard errors decrease. Through numerical simulations, we notice that, for  $N = 200$ , the maximum standard error [6] and relative error [16] in the velocity concerning time throughout all locations turns out to be approximately 0.009 and 2%, respectively. Hence, a good numerical result can be achieved with  $N = 200$  in this case. We set  $N = 200$  in all the following numerical experiments.

Figure 2 (b) presents the time evolution of the simulated velocity at  $y = 0.2, 0.4, 0.6, 0.8$  for the micro-macro model with  $N = 200$  particles, compared to the analytical solution (solid line). It shows our particle scheme with particle number  $N = 200$  yielded good numerical results.

#### 4.2. FENE model: Hysteresis behavior in simple extensional flows

The FENE models account for the finite extensibility of polymer chains, and can capture the hysteresis behavior of dilute polymer solutions in simple extensional flows during relaxation, which can be observed through the normal stress or elongational viscosity versus mean-square extension [67, 7, 8]. However, many macroscopic closure models for the FENE potential fail to capture this behavior [41, 8]. In this subsection, we demonstrate that the deterministic particle scheme is capable of capturing the hysteresis behavior of a FENE model.

We consider the elongational velocity gradient given by [6]:

$$\boldsymbol{\kappa}(t) = \boldsymbol{\varepsilon}(t) \text{diag}(1, -1) , \quad (60)$$

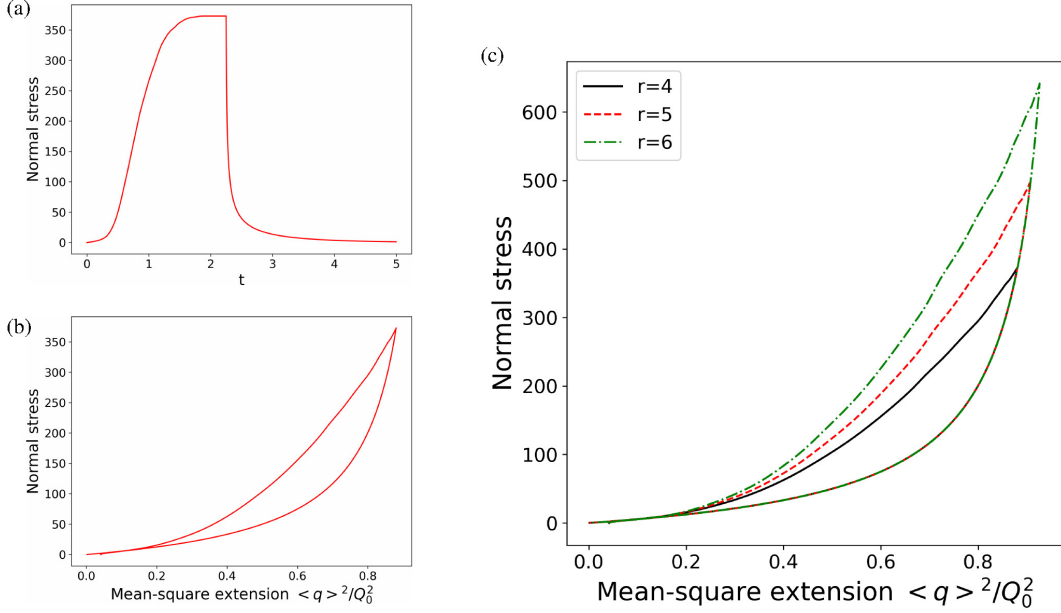


**Figure 3:** The start-up case with  $r = 4$ : (a) the time evolution and (b) the hysteresis of normal stress  $\tau_{11} - \tau_{22}$ ; (c) the hysteresis of the normal stress when  $r = 4, 5$  and  $6$ .

where  $\varepsilon(t)$  is the strain rate and  $\text{diag}(1, -1)$  is the  $2 \times 2$  diagonal matrix with diagonal entries being 1 and  $-1$ . Two cases of  $\varepsilon(t)$  will be considered. The start-up cases, with  $\varepsilon(t)$  given by

$$\varepsilon(t) = \begin{cases} r & 0 \leq t \leq \frac{9}{r}, \\ 0 & \text{otherwise.} \end{cases} \quad (61)$$

and the constant-gradient velocity case with

$$\varepsilon(t) = r. \quad (62)$$

The numerical simulations are carried out in given velocity gradient  $\nabla \mathbf{u} = \boldsymbol{\kappa}(t)$ . So, the Fokker-Planck equation can be reduced to

$$f_t + \nabla_{\mathbf{q}} \cdot (\boldsymbol{\kappa}(t) \mathbf{q} f) = \frac{1}{2W_i} \nabla_{\mathbf{q}} \cdot (f \nabla_{\mathbf{q}} \Psi) + \frac{1}{2W_i} \Delta_{\mathbf{q}} f. \quad (63)$$

where the distribution functions  $f = f(\mathbf{q}, t)$  is spatial homogeneous. The reduced Fokker-Planck equation (63) is employed for investigating the hysteresis behavior of FENE models.

Throughout this subsection, the initial data of particles is sampled from the 2-dimensional standard normal distribution. As stated in Section 4.1, we set kernel bandwidth  $h^2 = \text{med}^2 / \log N$  for Hookean models, where  $\text{med}$  is the median of the pairwise distance between the particles  $\{\mathbf{q}_i^n\}_{i=1}^N$ . However, this approach is not suitable for the FENE potential, as the equilibrium distributions are no longer Gaussian type and the median of the pairwise distance can become very large. Numerical experiments show that taking kernel bandwidth  $h = 0.01$  produces a good result for  $N = 200$  for the FENE model in simple extension flows. We also fix kernel bandwidth  $h = 0.01$  and  $N = 200$  for the following numerical experiments of the FENE models. We'll explore the effects of different kernel bandwidth  $h$  in future work.

For the start-up case, the time evolution of normal stress  $\tau_{11} - \tau_{22}$  and the plot of the normal stress versus the mean-square extension  $\langle \mathbf{q}^2 \rangle / Q_0^2$  for  $r = 4$  are plotted in Figure 3 (a)-(b). The comparison of hysteresis behavior of the FENE model for different extensional flow rates ( $r = 4, 5, 6$ ) is shown in Figure

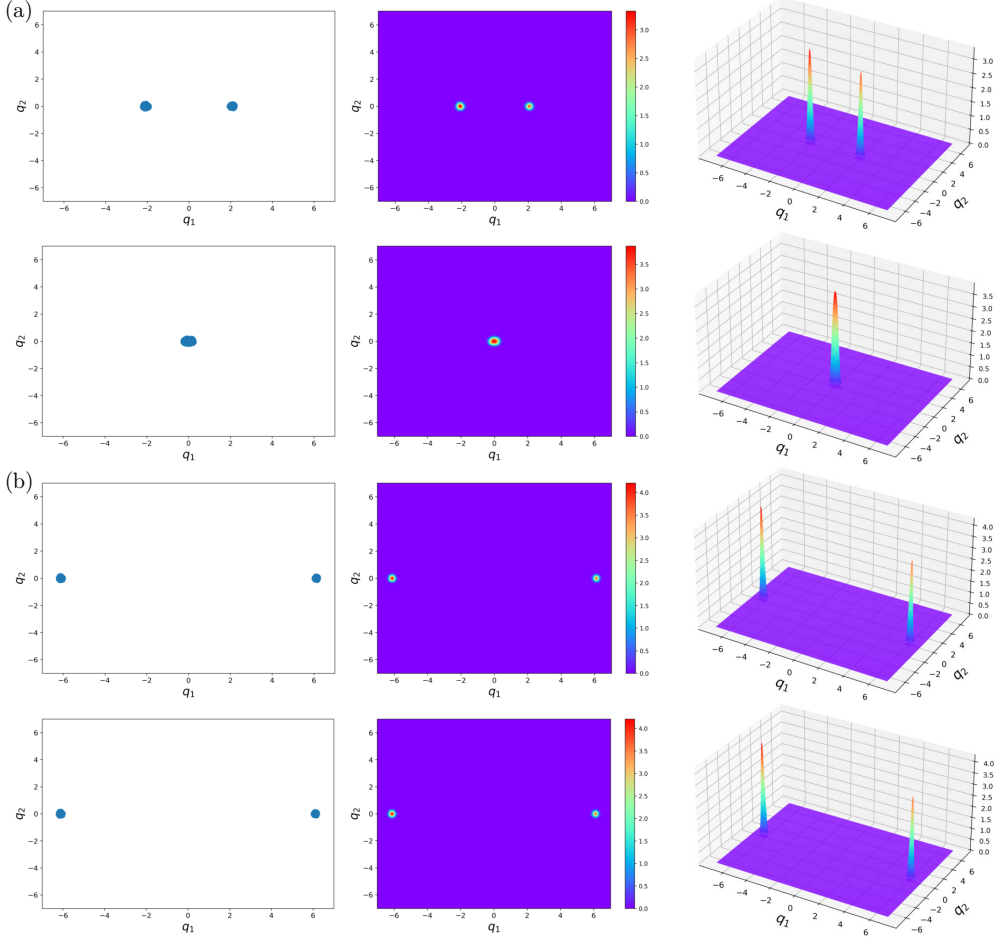


**Figure 4:** The position of particles (left) and the underlying distribution of particles obtained by kernel density estimation (middle and right) in the configuration space at different times with  $r = 4$ . (a) Start-up case at  $t = 3$  (the first row) and  $t = 8$  (the second row). (b) The constant-gradient velocity case at  $t = 3$  (the first row) and  $t = 8$  (the second row).

3 (c). It is observed that when the strength of velocity gradient is getting smaller, the hysteresis behavior becomes narrower. The numerical results are consistent with those obtained in the former work [41].

As discussed in [41], to catch the hysteresis of the original FENE model, a coarse-grained model should be able to catch the spike-like behaviors of the probability density in the FENE model in the large extensional effect of the flow field. The peak positions of the probability distribution function (PDF) distribution of the FENE model depend on the macroscopic flow field and change in time under the large macroscopic flow effects [40]. We show the position of particles (blue markers) and their underlying distribution probability density (obtained by the kernel density estimation) in the configuration space at different times ( $t = 3$  and  $t = 8$ ) for both the start-up case and the constant-gradient velocity case with  $r = 4$  in Figure 4. In the start-up case, the distribution splits into two spikes and then shows gradual centralized behavior. Eventually, it forms a single peak in the center, as shown in Figure 4 (a). Notice that the numerical results in the equilibrium state are consistent with the equilibrium solution of the Fokker-Planck equation with zero flow rate, as the velocity rate turns to zero when  $t$  is big enough ( $t > 9/r$ ). In the constant-gradient velocity case, the particles show two regions of higher concentration near the boundary of the configuration domain at the equilibrium state (i.e., with stable double spikes), as shown in Figure 4 (b). The numerical results show that the deterministic particle method can capture the  $\delta$ -function-like spike in the FENE model.

#### 4.3. FENE model: Simple shear flow

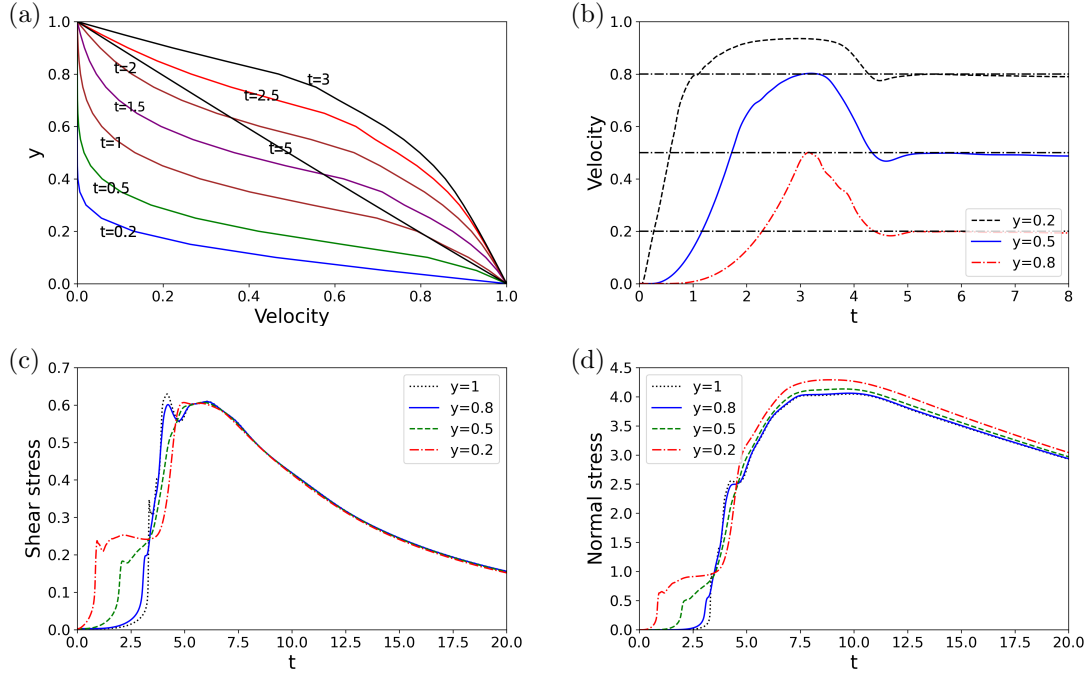


**Figure 5:** For the FENE model: the velocity  $u$  with respect to location  $y$  at different times (a); the time evolution of the velocity  $u$  at different locations (b); the time evolution of the shear stress(c) and normal stress difference(d) at location  $y = 0.2$ ,  $y = 0.5$ ,  $y = 0.8$  and  $y = 1$ .

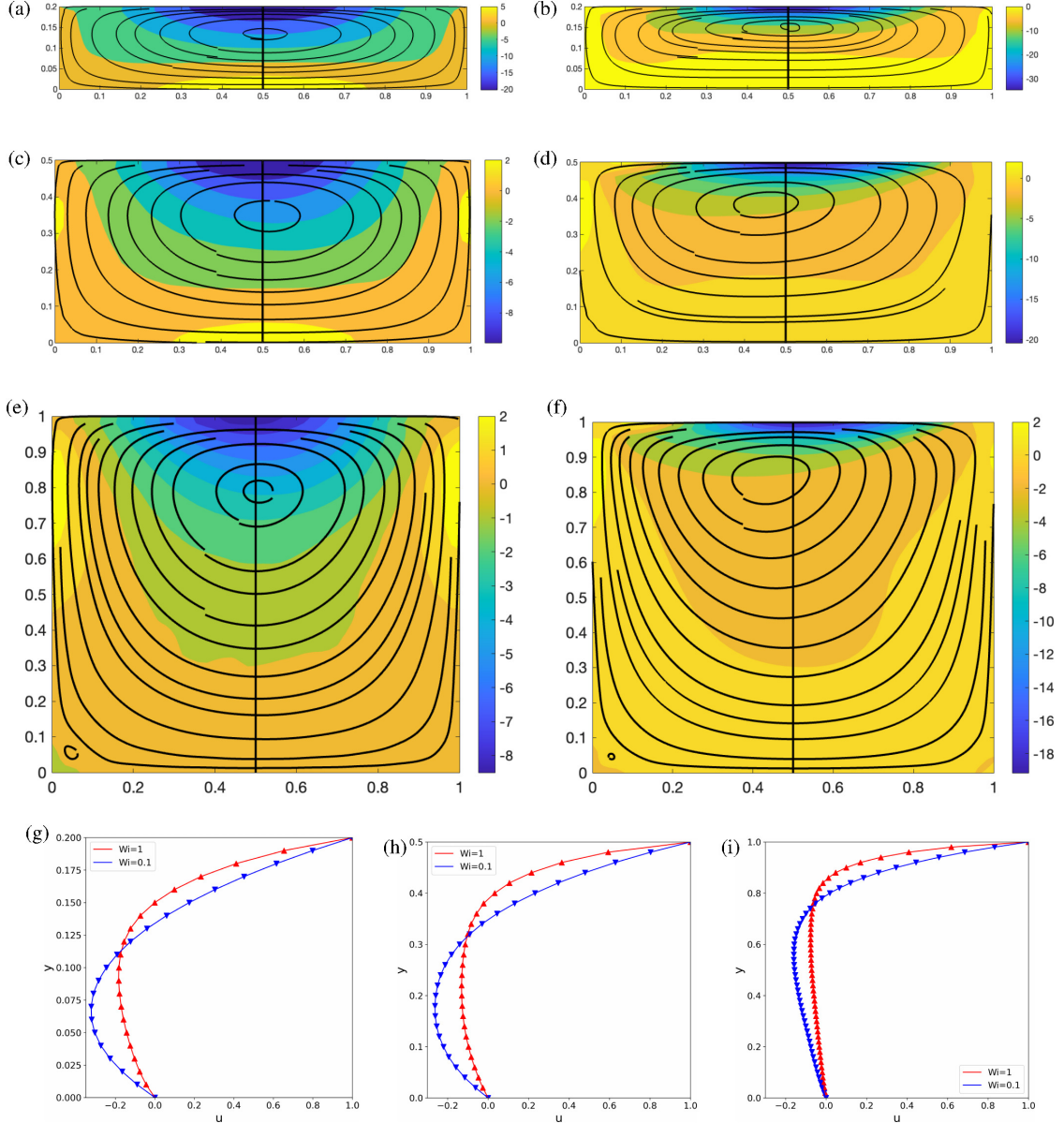
In this subsection, we evaluate the proposed algorithm's performance for the micro-macro model with a FENE potential in a start-up plane Couette flow as shown in Figure 1(a). We set  $L = 1$ ,  $M = 20$ ,  $\Delta t = 10^{-3}$ . The non-dimensional parameters are chosen to be  $\text{Re} = 1.2757$ ,  $\tilde{\eta}_s = 0.0521$ ,  $\text{Wi} = 49.62$ ,  $\epsilon_p = 0.9479$ , and  $b = \sqrt{50}$ , which are the same as those used in Ref. [17].

Figure 5 (a) shows the velocity evolution with respect to the location  $y$  at different times. It reveals the velocity overshoot phenomenon for the FENE model, which is a typical property of viscoelastic fluids. Figure 5 (b) displays the velocity evolution with respect to time  $t$  at three locations  $y = 0.2$ ,  $y = 0.5$  and  $y = 0.8$ . It can be seen that the velocity overshoot occurs sooner in fluid layers nearer to the moving plane. Figures 5(c-d) show the temporal evolution of the shear stress and the normal stress difference at different locations  $y = 0.2$ ,  $y = 0.5$ ,  $y = 0.8$ , and  $y = 1$ . The stress response is sharper in fluid layers nearer to the moving plane, which is consistent with the behavior of velocity overshoot. We observe that the maximum of the normal stress occurs after the maximum of the shear stress. Specifically, the shear stress of the FENE model reaches its maximum at around  $t = 6$ , but the maximum of the normal stress is reached at about  $t = 10$ . The numerical results agree well with the former work [17, 25], indicating the accuracy of our numerical scheme in the FENE case. Moreover, compared with the former work, our numerical results obtained by the deterministic particle scheme show fewer oscillations.

#### 4.4. FENE model: Lid driven cavity flow

In this subsection, we simulate the FENE model for lid-driven cavity flows (see Figure 1(b)). It is a 2D problem and a full 2D Navier-Stokes equation needs to be solved. Our experiments consider rectangular cavities with different heights:  $L_y = 0.2$ ,  $0.5$ , and  $1$ . To avoid numerical difficulties that arise from the geometric singularity at the edges of an idealized lid-driven cavity, we adopt a regularized horizontal lid velocity [68] of the form:

$$u(x) = 16U(x/L_x)^2(1 - x/L_x)^2.$$



**Figure 6:** The streamlines and vortices contour of the lid-driven cavity flow in the FENE case at  $T = 1$  with  $L_y = 0.2$  ((a):  $Wi = 0.1$ ; (b):  $Wi = 1$ ),  $L_y = 0.5$  ((c):  $Wi = 0.1$ ; (d):  $Wi = 1$ ) and  $L_y = 1$  ((e):  $Wi = 0.1$ ; (f):  $Wi = 1$ ). The profile of  $u$ -velocity with respect to  $y$  at position  $x = 0.5$  for  $Wi = 0.1, 1$  with  $L_y = 0.2$  (left),  $L_y = 0.5$  (middle) and  $L_y = 1$  (right).

To discretize the problem spatially, we choose  $\mathcal{T}_h$  to be a uniform triangular mesh with the mesh size  $N_x = 50, N_y = 20$  for  $L_y = 0.2$ ,  $N_x = 50, N_y = 25$  for  $L_y = 0.5$ , and  $N_x = 50, N_y = 50$  for  $L_y = 1$ . We set the time step size  $\Delta t = 10^{-3}$  for temporal discretization. Unlike the shear flow cases, the convection term  $\mathbf{u} \cdot \nabla \mathbf{q}$  is non-zero, which is dealt with by a Lagrangian approach as introduced in Section 3. Other parameters in the numerical experiments are set as follows:  $Re = 1$ ;  $\tilde{\eta}_s = 0.11$ ;  $\epsilon_p = 0.889$ ;  $b = \sqrt{50}$ .

Figures 6(a)-(f) display the streamlines and vortices contours for different  $L_y$  at time  $T = 1$  with  $Wi = 0.1$  and  $Wi = 1$ . Notice that the streamlines show symmetry structure when  $Wi = 0.1$ . And this symmetry structure holds for different  $L_y$ . However, as elasticity becomes more important, namely, the Weissenberg number ( $Wi$ ) increases, the symmetries in the streamline structures break due to the presence of elastic

effects [69]. Meanwhile, as the flow becomes asymmetric, the vortex center in the cavity shifts progressively upward and opposite to the direction of lid motion [39]. This phenomenon is more evident in Figures 6(g)-(i), which plot the  $u$ -velocity profiles at  $x = 0.5$  for the cavity flow with different  $L_y$  and  $Wi$ . Additionally, the introduction of elasticity also weakens the strengths of vortices near the moving lid [68].

The numerical results indicate that the particle-based scheme can capture these complex behaviors. The qualitative agreement between our simulation results and those of the former work [25, 39] validates our numerical scheme for the 2D lid-driven cavity flow case.

## 5. Conclusion

In this article, we present a novel deterministic particle-finite element method (FEM) discretization for micro-macro models of dilute polymeric fluids. The proposed scheme employs a finite element method for the fluid flow equation and a variational particle scheme used for the kinetic viscoelastic model. The proposed scheme is validated through various benchmark problems, including steady flow, shear flow, and 2D lid-driven cavity flow. Our numerical results are in excellent agreement with those from the former work [17, 25, 39, 40, 41] and demonstrate that the proposed scheme can capture certain complex behaviors of the nonlinear FENE model, including the hysteresis and  $\delta$ -function like spike behavior in extension flows [40, 41], velocity overshoot phenomenon in pure shear flow [17], symmetries breaking, vortex center shifting and vortices weakening in lid-driven cavity flow [25]. Compared with the stochastic simulation methods in the former work [16, 17, 25], where a large ensemble of realizations of the stochastic process is needed, the deterministic particle scheme can achieve good numerical results with reduced oscillations using only a small number of particles.

The proposed method can also be applied to other complex fluid models, such as the Doi-Onsager model for liquid crystal polymers [70], the multi-bead spring model [71], and a two-species model for wormlike micellar solutions [72, 73], which involves a reaction in the microscopic equation. Additionally, as a direction for future work, we aim to develop an energy-stable scheme for the overall system.

## Acknowledgement

This work is partially supported by the National Science Foundation (USA) grants NSF DMS-1950868, NSF DMS-2153029 (C. Liu, Y. Wang). Part of this work was done when X. Bao visited the Department of Applied Mathematics at the Illinois Institute of Technology, she would like to acknowledge the hospitality of IIT. X. Bao also would like to thank Prof. Rui Chen for the helpful discussions.

## Declaration of generative AI and AI-assisted technologies in the writing process

During the preparation of this work, the author(s) used ChatGPT in order to improve Language only. After using this tool/service, the author(s) reviewed and edited the content as needed and take(s) full responsibility for the content of the publication.

## References

- [1] C. Liu, An introduction of elastic complex fluids: an energetic variational approach, in: *Multi-Scale Phenomena in Complex Fluids: Modeling, Analysis and Numerical Simulation*, World Scientific, 2009, pp. 286–337.
- [2] R. Bird, C. Curtiss, R. Armstrong, O. Hassager, *Dynamics of Polymeric Liquids, Kinetic Theory (Dynamics of Polymer Liquids, vol. 1 and 2)*, Wiley-Interscience, New York, 1987.
- [3] R. Larson, *The Structure and Rheology of Complex Fluids*, Oxford University Press, Oxford, 1998.
- [4] C. L. Bris, T. Lelièvre, Micro-macro models for viscoelastic fluids: modelling, mathematics and numerics, *Sci. China Math.* 55 (2) (2012) 353–384.
- [5] T. Li, P. Zhang, Mathematical analysis of multi-scale models of complex fluids, *Commun. Math. Sci.* 5 (1) (2007) 1–51.
- [6] R. Keunings, On the Peterlin approximation for finitely extensible dumbbells, *J. Non-Newtonian Fluid Mech.* 68 (1997) 85–100.

[7] G. Lielens, P. Halin, I. Jaumain, R. Keunings, V. Legat, New closure approximations for the kinetic theory of finitely extensible dumbbells, *J. Non-Newtonian Fluid Mech.* 76 (1998) 249–279.

[8] R. Sizaire, G. Lielens, I. Jaumain, R. Keunings, V. Legat, On the hysteretic behaviour of dilute polymer solutions in relaxation following extensional flow, *J. Non-Newtonian Fluid Mech.* 82 (1999) 233–253.

[9] R. Bird, H. Öttinger, Transport properties of polymeric liquids, *Annu. Rev. Phys. Chem.* 43 (1) (1992) 371–406.

[10] J. Oldroyd, On the formulation of rheological equations of state, *Proc. R. Soc. Lond. A* 200 (1950) 523–541.

[11] A. Peterlin, Hydrodynamics of macromolecules in a velocity field with longitudinal gradient, *J. Polymer Sci., B* 4 (4) (1966) 287–291.

[12] M. Giga, A. Kirshtein, C. Liu, Variational modeling and complex fluids, *Handbook of mathematical analysis in mechanics of viscous fluids* (2017) 1–41.

[13] F. Lin, C. Liu, P. Zhang, On a micro-macro model for polymeric fluids near equilibrium, *Comm. Pure Appl. Math.* 60 (6) (2007) 838–866.

[14] W. E, W. Ren, E. Vanden-Eijnden, A general strategy for designing seamless multiscale methods, *J. Comput. Phys.* 228 (15) (2009) 5437–5453.

[15] P. Halin, G. Lielens, R. Keunings, V. Legat, The Lagrangian particle method for macroscopic and micro-macro viscoelastic flow computations, *J. Non-Newtonian Fluid Mech.* 79 (1998) 387–403.

[16] M. Hulsen, A. van Heel, B. van den Brule, Simulation of viscoelastic flows using Brownian configuration fields, *J. Non-Newtonian Fluid Mech.* 70 (1997) 79–101.

[17] M. Laso, H. Öttinger, Calculation of viscoelastic flow using molecular models: The CONNFFESSIT approach, *J. Non-Newtonian Fluid Mech.* 47 (1993) 1–20.

[18] A. Lozinski, R. G. Owens, T. N. Phillips, The Langevin and Fokker–Planck equations in polymer rheology, *Handbook of Numerical Analysis* 16 (2011) 211–303.

[19] H. Öttinger, *Stochastic Processes in Polymeric Fluids, Tools and Examples for Developing Simulation Algorithms*, Springer-Verlag, Berlin, 1996.

[20] S. Boyaval, T. Lelièvre, A variance reduction method for parametrized stochastic differential equations using the reduced basis paradigm, *Commun. Math. Sci.* 8 (3) (2010) 735–762.

[21] C. Chauvière, A new method for micro-macro simulations of viscoelastic flows, *SIAM J. Sci. Comput.* 23 (6) (2002) 2123–2140.

[22] M. Griebel, A. Rüttgers, Multiscale simulations of three-dimensional viscoelastic flows in a square–square contraction, *J. Non-Newtonian Fluid Mech.* 205 (2014) 42–63.

[23] B. Jourdain, C. L. Bris, T. Lelièvre, On a variance reduction technique for micro-macro simulations of polymeric fluids, *J. Non-Newtonian Fluid Mech.* 122 (2004) 91–106.

[24] A. P. Koppol, R. Sureshkumar, B. Khomami, An efficient algorithm for multiscale flow simulation of dilute polymeric solutions using bead-spring chains, *J. Non-Newtonian Fluid Mech.* 141 (2007) 180–192.

[25] X. Xu, J. Ouyang, W. Li, Q. Liu, SPH simulations of 2D transient viscoelastic flows using Brownian configuration fields, *J. Non-Newtonian Fluid Mech.* 208–209 (2014) 59–71.

[26] C. Chauvière, A. Lozinski, Simulation of dilute polymer solutions using a Fokker-Planck equation, *Comput. Fluids* 33 (2004) 687–696.

[27] D. Knezevic, E. Süli, A heterogeneous alternating-direction method for a micro-macro dilute polymeric fluid model, *M2AN Math. Model. Numer. Anal.* 43 (6) (2009) 1117–1156.

[28] A. Lozinski, C. Chauvière, A fast solver for Fokker-Planck equation applied to viscoelastic flows calculations: 2D FENE model, *J. Comput. Phys.* 189 (2003) 607–625.

[29] J. Shen, H. Yu, On the approximation of the Fokker–Planck equation of the finitely extensible nonlinear elastic dumbbell model I: A new weighted formulation and an optimal spectral-Galerkin algorithm in two dimensions, *SIAM J. Numer. Anal.* 50 (3) (2012) 1136–1161.

[30] J. Suen, Y. L. Joo, R. Armstrong, Molecular orientation effects in viscoelasticity, *Annu. Rev. Fluid Mech.* 34 (2002) 417–444.

[31] A. Ammar, Lattice Boltzmann method for polymer kinetic theory, *J. Non-Newtonian Fluid Mech.* 165 (2010) 1082–1092.

[32] L. Bergamasco, S. Izquierdo, A. Ammarb, Direct numerical simulation of complex viscoelastic flows via fast lattice-Boltzmann solution of the Fokker-Planck equation, *J. Non-Newtonian Fluid Mech.* 201 (2013) 29–38.

[33] G. Russo, Deterministic diffusion of particles, *Comm. Pure Appl. Math.* 43 (6) (1990) 697–733.

[34] P. Degond, F.-J. Mustieles, A deterministic approximation of diffusion equations using particles, *SIAM J. Sci. Statist. Comput.* 11 (2) (1990) 293–310.

[35] G. Lacombe, S. Mas-Gallic, Presentation and analysis of a diffusion-velocity method, in: *ESAIM: Proc.*, Vol. 7, EDP Sciences, 1999, pp. 225–233.

[36] J. A. Carrillo, K. Craig, F. S. Patacchini, A blob method for diffusion, *Calc. Var.* 58 (2) (2019) 53.

[37] Y. Wang, J. Chen, L. Kang, C. Liu, Particle-based energetic variational inference, *Stat. Comput.* 31 (3) (2021) Paper No. 34, 17pp.

[38] C. Liu, Y. Wang, On Lagrangian schemes for porous medium type generalized diffusion equations: A discrete energetic variational approach, *J. Comput. Phys.* 417 (2020) 109566.

[39] A. Grillet, B. Yang, B. Khomami, E. Shaqfeh, Modeling of viscoelastic lid driven cavity flow using finite element simulations, *J. Non-Newtonian Fluid Mech.* 88 (1999) 99–131.

[40] Y. Hyon, Q. Du, C. Liu, An enhanced macroscopic closure approximation to the micro-macro fene model for polymeric materials, *Multiscale Model. Simul.* 7 (2) (2008) 978–1002.

[41] Y. Hyon, Hysteretic behavior of a moment-closure approximation for fene model, *Kinet. Relat. Mod.* 7 (3) (2014) 493–507.

[42] L. Rayleigh, Some general theorems relating to vibrations, *Proc. Lond. Math. Soc.* 1 (1) (1871) 357–368.

[43] L. Onsager, Reciprocal relations in irreversible processes. I., *Phys. Rev.* 37 (4) (1931) 405.

[44] L. Onsager, Reciprocal relations in irreversible processes. II., *Phys. Rev.* 38 (12) (1931) 2265.

[45] Y. Wang, C. Liu, P. Liu, B. Eisenberg, Field theory of reaction-diffusion: law of mass action with an energetic variational approach, *Phys. Rev. E* 102 (6) (2020) 062147, 9 pp.

[46] J. L. Ericksen, Reversible and nondissipative processes, *Quart. J. Mech. Appl. Math.* 45 (4) (1992) 545–554.

[47] V. Arnold, Mathematical methods of classical mechanics, *Graduate Texts in Mathematics*, 60. Springer-Verlag, New York, 2013.

[48] F. Lin, Some analytical issues for elastic complex fluids, *Comm. Pure Appl. Math.* 65 (7) (2012) 893–919.

[49] Y. Epshteyn, C. Liu, C. Liu, M. Mizuno, Nonlinear inhomogeneous fokker–planck models: energetic-variational structures and long-time behavior, *Anal. Appl.* 20 (6) (2022) 1295–1356.

[50] J. L. Ericksen, On the cauchy-born rule, *Math. Mech. Solids* 13 (3-4) (2008) 199–220.

[51] X. Bao, R. Chen, H. Zhang, Constraint-preserving energy-stable scheme for the 2d simplified ericksen-leslie system, *J. Comput. Math.* 39 (1) (2021) 1–21.

[52] R. Becker, X. Feng, A. Prohl, Finite element approximations of the ericksen-leslie model for nematic liquid crystal flow, *SIAM J. Numer. Anal.* 46 (4) (2008) 1704–1731.

[53] R. Chen, G. Ji, X. Yang, H. Zhang, Decoupled energy stable schemes for phase-field vesicle membrane model, *J. Comput. Phys.* 302 (2015) 509–523.

[54] J. L. Guermond, P. Minev, J. Shen, An overview of projection methods for incompressible flows, *Comput. Methods Appl. Mech. Engrg.* 195 (44–47) (2006) 6011–6045.

[55] F. Brezzi, M. Fortin, *Mixed and Hybrid Finite Element Methods*, Springer-Verlag, 1991.

[56] M. Tabata, D. Tagami, Error estimates for finite element approximations of drag and lift in nonstationary navier-stokes flows, *Jpn. J. Ind. Appl. Math.* 17 (2000) 371–389.

[57] D. Boffi, F. Brezzi, M. Fortin, *Mixed Finite Element Methods and Applications*, Springer Series in Computational Mathematics, 44, Springer, Heidelberg, 2013.

[58] B. Jourdain, T. Lelièvre, C. L. Bris, Numerical analysis of micro-macro simulations of polymeric fluid flows: a simple case, *Math. Mod. Meth. Appl. S.* 12 (9) (2002) 1205–1243.

[59] Q. Du, C. Liu, P. Yu, FENE dumbbell model and its several linear and nonlinear closure approximations, *Multiscale Model. Simul.* 4 (3) (2005) 709–731.

[60] H. Öttinger, B. V. D. Brule, M. Hulsen, Brownian configuration fields and variance reduced connffessit, *J. Non-Newtonian Fluid Mech.* 70 (3) (1997) 255–261.

[61] C. Helzel, F. Otto, Multiscale simulations for suspensions of rod-like molecules, *J. Comput. Phys.* 216 (1) (2006) 52–75.

[62] R. T. Rockafellar, Monotone operators and the proximal point algorithm, *SIAM journal on control and optimization* 14 (5) (1976) 877–898.

[63] J. Barzilai, J. M. Borwein, Two-point step size gradient methods, *IMA journal of numerical analysis* 8 (1) (1988) 141–148.

[64] M. Arroyo, M. Ortiz, Local maximum-entropy approximation schemes: a seamless bridge between finite elements and meshfree methods, *Int. J. Numer. Meth. Engng.* 65 (2006) 2167–2202.

[65] A. Rosolen, C. Peco, M. Arroyo, An adaptive meshfree method for phase-field models of biomembranes. part i: Approximation with maximum-entropy basis functions, *J. Comput. Phys.* 249 (2013) 303–319.

[66] Q. Liu, D. Wang, Stein variational gradient descent: A general purpose bayesian inference algorithm, *Adv. Neural Inf. Process. Syst.* 29 (2016).

[67] P. S. Doyle, E. S. Shaqfeh, G. H. McKinley, S. H. Spiegelberg, Relaxation of dilute polymer solutions following extensional flow, *J. Non-Newtonian Fluid Mech.* 76 (1998) 79–110.

[68] R. Sousa, R. Poole, A. Afonso, F. Pinho, P. Oliveira, A. Morozov, M. Alves, Lid-driven cavity flow of viscoelastic liquids, *J. Non-Newtonian Fluid Mech.* 234 (2016) 129–138.

[69] S. Dalal, G. Tomar, P. Dutta, Numerical study of driven flows of shear thinning viscoelastic fluids in rectangular cavities, *J. Non-Newtonian Fluid Mech.* 229 (2016) 59–78.

[70] M. Doi, S. F. Edwards, *The theory of polymer dynamics*, Vol. 73, oxford university press, 1988.

[71] Q. Zhou, R. Akhavan, Cost-effective multi-mode fene bead-spring models for dilute polymer solutions, *J. Non-Newtonian Fluid Mech.* 116 (2–3) (2004) 269–300.

[72] C. Liu, Y. Wang, T.-F. Zhang, Global existence of classical solutions for a reactive polymeric fluid near equilibrium, *Calc. Var. Partial Differential Equations* 61 (2022) Paper No. 117, 37 pp.

[73] Y. Wang, T.-F. Zhang, C. Liu, A two species micro–macro model of wormlike micellar solutions and its maximum entropy closure approximations: An energetic variational approach, *J. Non-Newtonian Fluid Mech.* 293 (2021) 104559.